

# TRANSITION FROM REGULAR TO CHAOTIC CIRCULATION IN MAGNETIZED CORONAE NEAR COMPACT OBJECTS

O. KOPÁČEK, V. KARAS

Astronomical Institute, Academy of Sciences, Boční II 1401, CZ-141 31 Prague, Czech Republic.

J. KOVÁŘ, Z. STUHLÍK

Institute of Physics, Faculty of Philosophy and Science, Silesian University in Opava, Bezručovo nám. 13, CZ-746 01 Opava, Czech Republic.

*Draft version September 12, 2018*

## ABSTRACT

Accretion onto black holes and compact stars brings material in a zone of strong gravitational and electromagnetic fields. We study dynamical properties of motion of electrically charged particles forming a highly diluted medium (a corona) in the regime of strong gravity and large-scale (ordered) magnetic field.

We start our work from a system that allows regular motion, then we focus on the onset of chaos. To this end, we investigate the case of a rotating black hole immersed in a weak, asymptotically uniform magnetic field. We also consider a magnetic star, approximated by the Schwarzschild metric and a test magnetic field of a rotating dipole. These are two model examples of systems permitting energetically bound, off-equatorial motion of matter confined to the halo lobes that encircle the central body. Our approach allows us to address the question of whether the spin parameter of the black hole plays any major role in determining the degree of the chaoticity.

To characterize the motion, we construct the Recurrence Plots (RP) and we compare them with Poincaré surfaces of section. We describe the Recurrence Plots in terms of the Recurrence Quantification Analysis (RQA), which allows us to identify the transition between different dynamical regimes. We demonstrate that this new technique is able to detect the chaos onset very efficiently, and to provide its quantitative measure. The chaos typically occurs when the conserved energy is raised to a sufficiently high level that allows the particles to traverse the equatorial plane. We find that the role of the black-hole spin in setting the chaos is more complicated than initially thought.

*Subject headings:* acceleration of particles, black hole physics, magnetic fields, methods: numerical

## 1. INTRODUCTION

The role of magnetic fields near strongly gravitating objects has been subject of many investigations (e.g. Punsly 2008). They are relevant for accretion disks that may be embedded in large-scale magnetic fields, for example when the accretion flow penetrates close to a neutron star (Lipunov 1992; Mestel 1999). Outside the main body of the accretion disk, i.e. above and below the equatorial plane, the accreted material forms a highly diluted environment, a ‘corona’, where the density of matter is low and the mean free path of particles is large in comparison with the characteristic length-scale, i.e. the gravitational radius of the central body,  $R_g \equiv GM/c^2 \approx 1.5(M/M_\odot)$  km, where  $M$  is the central mass. The origin of the coronal flows and the relevant processes governing their structure are still unclear. In this context we discuss motion of electrically charged particles outside the equatorial plane.

Off-equatorial, energetically bound motion of charged particles in strong gravitational and electromagnetic fields is pertinent to the description of accretion disk coronae around black holes and compact (neutron) stars. In our previous papers (Kovář et al. 2008, 2010) we discussed the existence of energetically-bound stable orbits of charged particles occurring outside the equatorial plane, extending thus a large variety of complementary studies (e.g., Bičák et al. 1989; Stuchlík et al.

1999; Prasanna 1980; Prasanna & Sengupta 1994; Aliev & Özdemir 2001, and further references cited therein). Particles on off-equatorial stable trajectories form a coronal flow that is possible at certain radii and for certain combinations of the model parameters, namely, the specific charge of the particles, the conserved energy and the angular momentum of the particle motion, the strength and orientation of the magnetic field, and the spin of the central body.

We assume that the magnetic field permeating the corona has a large-scale (ordered) component (Bisnovaty-Kogan & Lovelace 2007). In this case, charged particles can be trapped in toroidal regions, extending symmetrically above and below the equatorial plane and forming two halo lobes. However, this trapping happens only for certain combinations of model parameters (Kovář et al. 2010).

We consider two types of the model setup: a rotating (Kerr) black hole in an asymptotically uniform magnetic field parallel to the symmetry axis (Wald 1974; Tomimatsu & Takahashi 2001; Koide 2004; Koide et al. 2006), and a non-rotating star (described by the Schwarzschild metric) endowed with a rotating magnetic dipole field (Pettersson 1975; Sengupta 1995). Both cases can be regarded as integrable systems with the electromagnetic field acting as a perturbation.

The above-mentioned lobes are defined by the figures

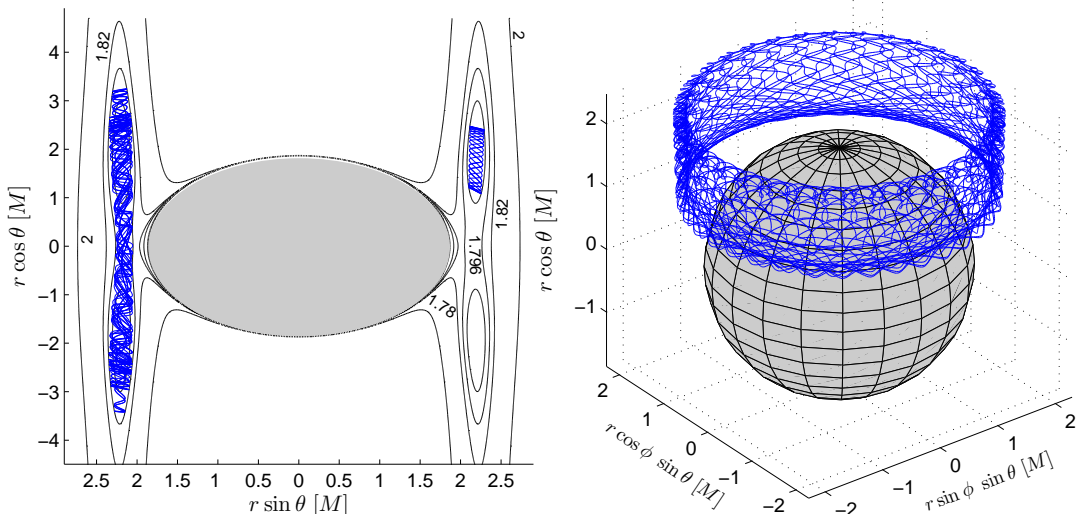


**Figure 1.** In the left panel we present a poloidal section of the selected isocontours of the effective potential  $V_{\text{eff}}(r, \theta)$ , eq. (5), for a charged particle ( $\tilde{q}\tilde{Q} = 2$ ,  $\tilde{L} = 5M$ ) on the Kerr background ( $a = 0.5M$ ). We assume the presence of Wald uniform magnetic field ( $\tilde{q}B_0 = 2M^{-1}$ ). The off-equatorial potential lobes are present, allowing stable motion. Two exemplary trajectories of test particles are shown – in the left lobe a chaotic orbit of energy  $\tilde{E} = 1.796$ , while in the right lobe the regular, purely off-equatorial trajectory of  $\tilde{E} = 1.78$ . Both particles were launched at  $r(0) = 3.11$ ,  $\theta(0) = \pi/4$  with  $u^r(0) = 0$  and their trajectories interweave with each other. We plot the poloidal  $(r, \theta)$  projection of the trajectory; what appears as a lobe in the poloidal plane is an axially symmetric 3-dimensional rotational structure. The latter is illustrated in the right panel where the case of the off-equatorial regular trajectory is shown.

of the effective potential in the poloidal plane. These were previously studied in the context of charge separation that is expected to occur in pulsar magnetospheres (e.g. Neukirch 1993). Here, we address whether the trajectories within these lobes are regular (i.e., whether the system is integrable), or if they instead exhibit a chaotic behavior. A related problem was studied recently by Takahashi & Koyama (2009) in an attempt to find a connection between chaoticness of the motion and the spin of a rotating black hole residing in the center. These authors suggest that chaotic behavior occurs for certain values of the black hole spin, while for others the system is indeed regular.

The idea of investigating the connection between the spin of a black hole and chaoticness of motion of matter near its horizon is very interesting for the following reason. Because of high degree of symmetry of the background spacetime, the unperturbed motion is regular (Carter 1968); no chaos is present. The electromagnetic perturbation may trigger the chaos, however, its effect can be expected to diminish very near the horizon, where strong gravity of the black hole should prevail. This is also the region where the spin effects are most prominent. Further out various other influences become important due to distant matter and the turbulence in accreted material. Therefore the connection between the spin and the motion chaoticness is best applicable in the immediate vicinity of the black hole, i.e. within the inner parts of corona.

The recurrence analysis (Marwan et al. 2007) provides us with a powerful tool for the investigation of complex dynamical systems. The method examines the recurrences of the system to the vicinity of previously reached phase space points. It has been typically adopted to study the experimental data, where often only some (if not just one) of the phase space variables are known from the measurements. Takens' embedding theorems (Takens 1981) are then used to reconstruct the phase space por-

trait of such a system. In our study we are equipped with the full phase space trajectory from the numerical integration of the equations of motion, so that we can use the recurrence analysis directly.

It appears that the method of Recurrence Plots has not been employed in the context of relativistic astrophysical systems yet. To this end, one needs a consistent definition of the neighborhood of a point in the phase space in a curved spacetime. Below, we discuss the phase space distance and suggest a form of the distance norm suitable in such circumstances.

The paper is organized as follows. In sec. 2 we review the equations of particle motion, which we then integrate to obtain trajectories. In sec. 3 we introduce the basic properties of Recurrence Plots. Sec. 4 analyses the motion around a Kerr black hole endowed with a uniform magnetic test field. We employ Poincaré surfaces of section and Recurrence Plots. The two approaches allow us to show the onset of chaos in different, complementary ways. We examine the motion in off-equatorial lobes, pay special attention to the spin dependence of the stability of motion, and we notice the emergence of ‘potential valleys’ that allow the particles to escape from the equatorial plane along a narrow collimated corridor. Analysis of the off-equatorial motion around a magnetic star is presented in sec. 5. We consider a dipole-type magnetic field, which sets different limits on the off-equatorial range of allowed motion of charged particles. It also defines different regimes of chaoticness in comparison with the uniform magnetic field. Finally, results of the analysis are summarized in sec. 6.

## 2. EQUATIONS OF MOTION AND THE EFFECTIVE POTENTIAL

The phase space trajectories of integrable systems are regular, meaning that they are bound to the surface of an  $n$ -dimensional torus, where  $n$  is the number of degrees of freedom. The torus is determined uniquely by

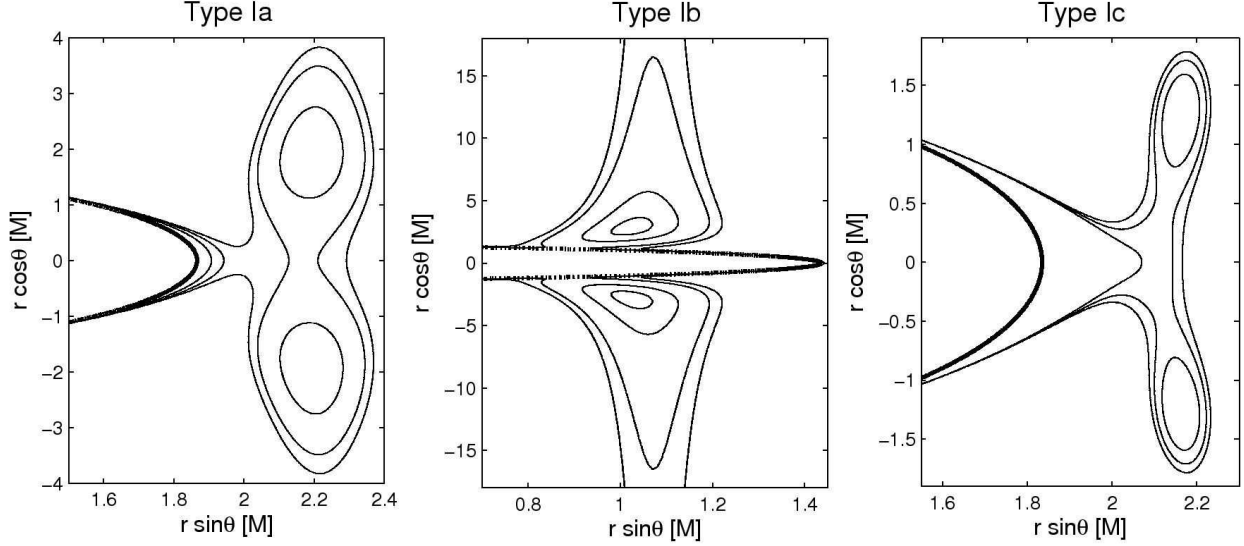


**Figure 2.** The overview of possible topologies of the off-equatorial potential structure above the event horizon (thick line in plots) of Kerr black hole endowed with the Wald test field.

$n$  constants of motion that are present in such a system. Its behavior can be explored by Poincaré surfaces of section, which are defined by intersections of the phase space trajectory with a 2-dimensional plane (Lichtenberg & Lieberman 1992). On the other hand, non-integrable chaotic systems generally have fewer integrals than the number of degrees of freedom. In general, both the regular and the chaotic orbits may coexist in the phase space of a single system.

Chaotic orbits are ergodic on the given hypersurface. Its dimension is now larger than  $n$ , and the section points thus fill areas in the plot of the Poincaré surface. However, depending on the initial conditions, regular orbits can also appear in non-integrable systems. Such orbits maintain the value of some additional constant of motion, although it is not generally possible to write this constant in an explicit form. In the context of motion around black holes perturbed by (weak) external sources, various aspects of chaos were studied e.g. by Karas & Vokrouhlický (1992); Nakamura & Ishizuka (1993); Podolský & Veselý (1998), and very recently by Semerák & Suková (2010).

A standard approach to an integrable system with a non-integrable perturbation assumes complete control over the strength of the perturbation (i.e., the perturbation can be set to be arbitrarily weak). If this were the case, we could first switch the perturbation completely off, analyze the orbits, and then observe the impact of gradually increasing the perturbation strength upon these orbits. However, the class of off-equatorial bound orbits only exists when the electromagnetic term is strong enough to balance the gravitational attraction of the central body. Then the (sufficiently strong) perturbation is by itself the cause of the new kind of the regular motion that happens outside the equatorial plane.

Having this delicacy on mind, we shall use the usual Hamiltonian formalism to express equations of motion governing the trajectories. We first construct the super-Hamiltonian  $\mathcal{H}$  (Misner et al. 1973),

$$\mathcal{H} = \frac{1}{2}g^{\mu\nu}(\pi_\mu - qA_\mu)(\pi_\nu - qA_\nu), \quad (1)$$

where  $m$  and  $q$  are the rest mass and charge of the test particle,  $\pi_\mu$  is the generalized (canonical) momentum,

$g^{\mu\nu}$  is the metric tensor, and  $A_\mu$  denotes the vector potential of the electromagnetic field. The latter is related to the electromagnetic tensor  $F_{\mu\nu}$  by  $F_{\mu\nu} = A_{\nu,\mu} - A_{\mu,\nu}$ . Unless otherwise stated, we will use geometrical units,  $G = c = 1$ .

The Hamiltonian equations are given as

$$\frac{dx^\mu}{d\lambda} \equiv p^\mu = \frac{\partial\mathcal{H}}{\partial\pi_\mu}, \quad \frac{d\pi_\mu}{d\lambda} = -\frac{\partial\mathcal{H}}{\partial x^\mu}, \quad (2)$$

where  $\lambda = \tau/m$  is the affine parameter,  $\tau$  denotes the proper time, and  $p^\mu$  is the standard kinematical four-momentum for which the first equation reads  $p^\mu = \pi^\mu - qA^\mu$ .

In the case of stationary and axially-symmetric systems, we identify two constants of motion, namely, the energy  $E$  and angular momentum  $L$ . From the second Hamiltonian equation (2) we obtain

$$\pi_t = p_t + qA_t \equiv -E \quad (3)$$

$$\pi_\phi = p_\phi + qA_\phi \equiv L. \quad (4)$$

The trajectory is specified by the integrals of motion  $E$ ,  $L$ , and the initial values  $r(0)$ ,  $\theta(0)$  and  $u^r(0)$ . The initial  $u^\theta(0)$  can be calculated from the normalization condition,  $g^{\mu\nu}u_\mu u_\nu = -1$  (we always choose the non-negative root).

The effective potential can be derived in the following form:

$$V_{\text{eff}} = \frac{-\beta + \sqrt{\beta^2 - 4\alpha\gamma}}{2\alpha}, \quad (5)$$

where

$$\alpha = -g^{tt}, \quad (6)$$

$$\beta = 2[g^{t\phi}(\tilde{L} - \tilde{q}A_\phi) - g^{tt}\tilde{q}A_t], \quad (7)$$

$$\gamma = -g^{\phi\phi}(\tilde{L} - \tilde{q}A_\phi)^2 - g^{tt}\tilde{q}^2 A_t^2 + 2g^{t\phi}\tilde{q}A_t(\tilde{L} - \tilde{q}A_\phi) - 1, \quad (8)$$

and where we introduce specific quantities  $\tilde{L} \equiv \frac{L}{m}$ ,  $\tilde{E} \equiv \frac{E}{m}$  and the specific charge  $\tilde{q} \equiv \frac{q}{m}$ . Local minima

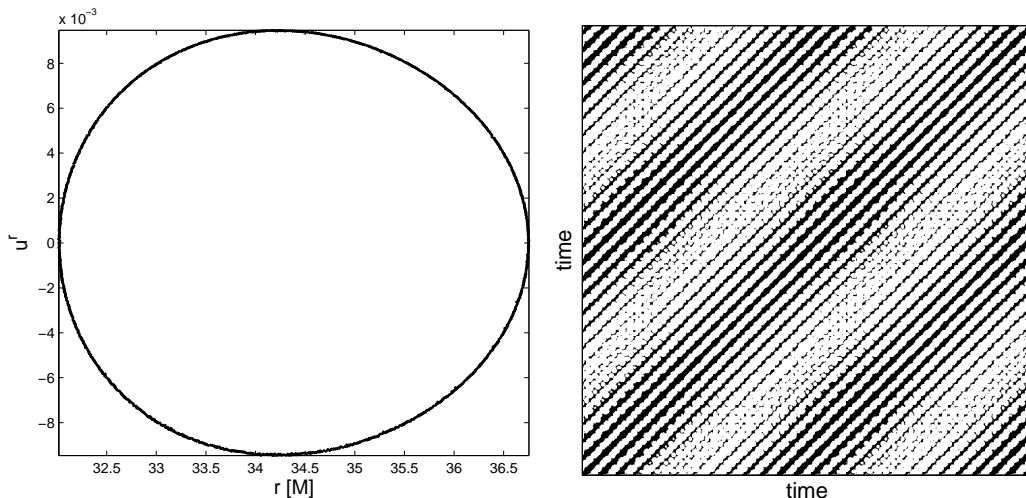


**Figure 3.** Regular motion in the equatorial potential lobe in the fully integrable system of charged test particle ( $\tilde{E} = 0.99$ ,  $\tilde{L} = 5M$ ,  $\tilde{q} = 10^4$ ,  $r(0) = 32.02 M$ ,  $\theta(0) = 1.54$ ) in the pure Kerr-Newman spacetime ( $\tilde{Q} = 3 \times 10^{-5}$ ,  $a = 0.5 M$ ) endowed with the fourth Carter constant of motion  $\mathcal{L}$ . Long diagonals parallel to the LOI are general hallmark of regularity in the RPs.

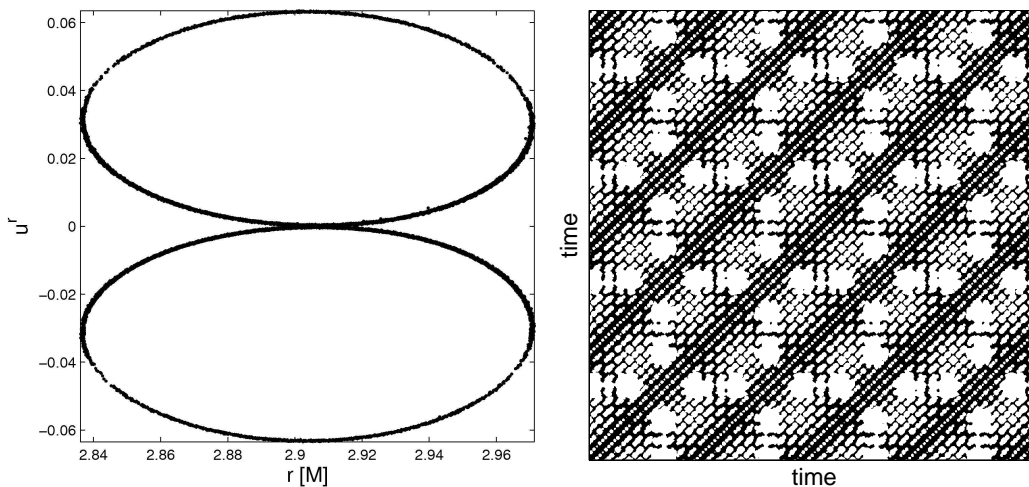


**Figure 4.** Regular off-equatorial motion of a charged test particle ( $\tilde{E} = 1.77$ ,  $\tilde{L} = 5M$ ,  $r(0) = 2.9 M$ ,  $\theta(0) = 0.856$  and  $u^r(0) = 0$ ) on the Kerr background ( $a = 0.5 M$ ) enriched with the Wald test field ( $\tilde{q}B_0 = 2M^{-1}$ ,  $\tilde{q}\tilde{Q} = 2$ ). The diagonal structures typical for trajectories in integrable systems are preserved, though the pattern is more complicated.

of  $V_{\text{eff}}(r, \theta)$  reflect the location of stable orbits of test particles. Off-equatorial potential minima were identified and various types of potential lobes were discussed elsewhere (see Kovář et al. 2010). We can express the effective potential (5) as a function of  $r$  and  $u^r$ , and use it to determine the boundaries of allowed regions in Poincaré surfaces of section for a given value of  $\theta$ .<sup>1</sup>

We employ the Kerr metric in standard Boyer-Lindquist coordinates  $t, r, \theta, \phi$  (Misner et al. 1973):

$$ds^2 = -\frac{\Delta}{\Sigma} (dt - a \sin^2 \theta d\phi)^2 + \frac{\sin^2 \theta}{\Sigma} [(r^2 + a^2) d\phi - a dt]^2 + \frac{\Sigma}{\Delta} dr^2 + \Sigma d\theta^2, \quad (9)$$

<sup>1</sup> We have employed the method of effective potential to study the stability of the motion, however, we note that the force formalism (Abramowicz et al. 1995; Kovář & Stuchlík 2007) can serve as a very efficient alternative tool. In particular, the off-equatorial motion of charged particles can be examined via the procedure described in Kovář et al. (2010). This allows us to localize minima of the effective potential around which the stable orbits occur.

where  $a$  stands for the spin parameter (the specific angular momentum,  $0 \leq a \leq M$ ),  $\Delta \equiv r^2 - 2Mr + a^2$ , and  $\Sigma \equiv r^2 + a^2 \sin^2 \theta$ . It is sufficient to consider positive values of  $a$  without loss of generality (the cases of prograde and retrograde motion are distinguished by the sign of the particle charge and the orientation of the magnetic field). By setting  $a = 0$  the metric reduces to the static one of the Schwarzschild spacetime.

At this point, a note is worth on the adopted computational scheme which we have employed to study the trajectories and to detect the chaotical behavior. In order to reach reliable results, we coded several approaches and we checked their stability and precision. We employ the multi-step Adams-Bashforth-Moulton solver to determine the phase-space trajectory by numerical integration of eqs. (2). In some cases, when a higher precision is demanded, we use the 7-8th order Dormand-Prince method that belongs to the family of explicit Runge-Kutta solvers with adaptive stepsize. This method improves the accuracy significantly, as can be verified by checking the conservation of the integrals of motion along

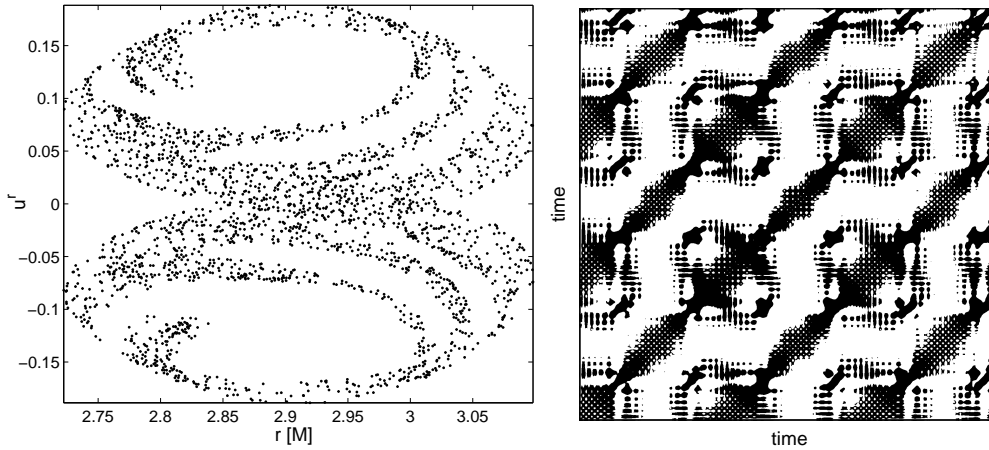


**Figure 5.** A transitional state between the regular and chaotic regimes of motion of a highly charged test particle which only differs from the previous case by increasing the energy to  $\tilde{E} = 1.796$ . The diagonal lines in the RP are partially disrupted, indicating the onset of chaos.

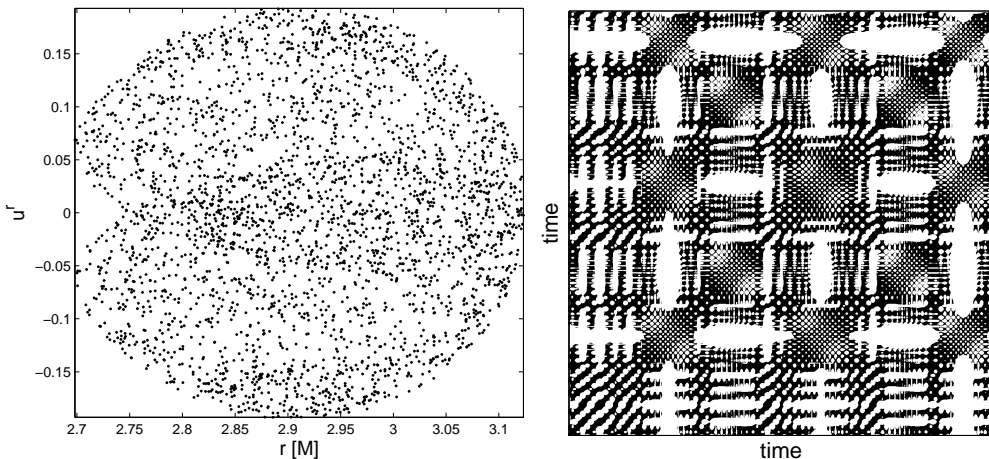


**Figure 6.** The chaotic motion of a highly charged test particle which only differs from the previous case by increasing the energy to  $\tilde{E} = 1.7975$ . The diagonal lines in the RP are now disrupted and complex large-scale structures appear which are a characteristic indication of deterministic chaos.

the trajectory. However, the improved accuracy comes at the expense of computational time, as the adopted Dormand-Prince scheme is more computationally demanding than the Adams-Bashforth-Moulton solver.

Furthermore, it is well-known that, when dealing with Hamiltonian systems, the most appropriate solvers are those which respect the symplectic nature of Hamiltonian dynamics (e.g. Yoshida 1993). We therefore employed also the implicit Gauss-Legendre Runge-Kutta (GLRK) method, which is a symplectic scheme. Indeed, we confirm that this code provides the most reliable results, especially in the case of long-term integration. The difference in the accuracy between GLRK and non-symplectic solvers reaches several orders of magnitude and it is generally more apparent in the case of chaotic trajectories, as expected. However, the cost in terms of the computational time is also non-negligible, and so we only use the GLRK method to achieve very accurate long-time determination of the trajectory in several exemplary runs.

### 3. RECURRENCE ANALYSIS

The Kerr metric is well-known and the analysis of test particle motion in this spacetime was carried out in many papers (Misner et al. 1973). Among important features of the Kerr metric is the fact that the particle trajec-

tories are integrable, and so the chaos can set in only when perturbations of the background gravitational field are introduced or additional electromagnetic interaction with fields of external sources are allowed. This is also where recurrence analysis can be helpful.

Methods of phase space recurrences have been successfully applied to a wide range of various empirical data, not only in physics but also related to physiology, geology, finances and other fields. Recurrence plots are especially suitable for the investigation of rather short and nonstationary data. On the other hand, the method of recurrence analysis has not yet been widely applied to study the dynamical properties of motion in relativistic systems. We thus briefly summarize this approach for our context.

Besides more traditional methods of the numerical analysis of dynamical systems, such as a visual survey of Poincaré surfaces of section or the evaluation of the Lyapunov spectra (Skokos 2010), the recurrence analysis is a rather novel technique, based on the analysis of recurrences of the system into the vicinity of its previous states.

Recurrence Plots (RP) are introduced as a tool of visualizing the recurrences of a trajectory in the phase space (Eckmann et al. 1987). The method is based on exam-

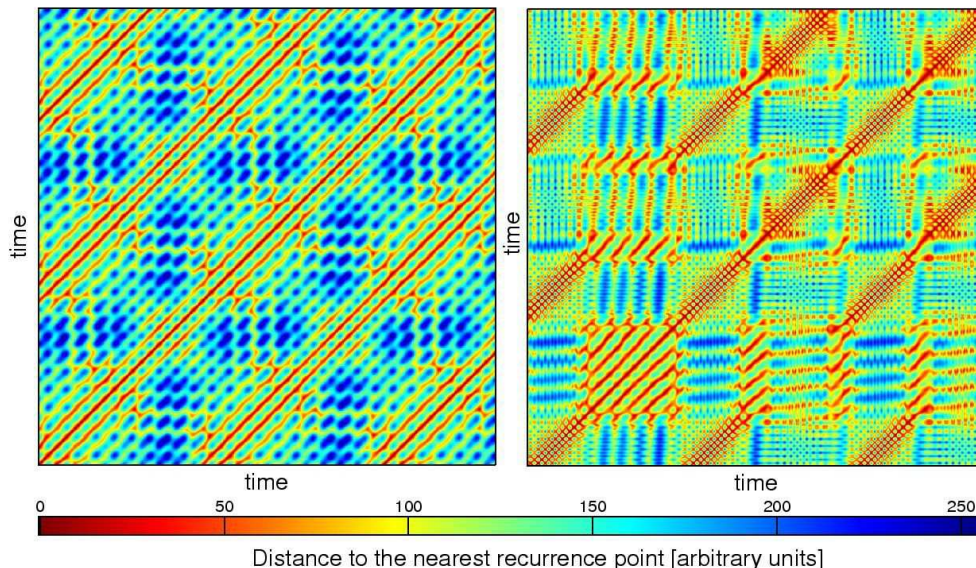


**Figure 7.** Color map of the distance in the phase space to the nearest recurrence point. This example concerns a charged particle trajectory near the Kerr black hole in the asymptotically uniform magnetic field. Left: the case of regular motion with the energy of  $\tilde{E} = 1.77$ . Right: the case of chaotic motion with  $\tilde{E} = 1.7975$ . In the latter case more complex structure appear in the recurrence plot. The common parameters of both panels are  $\tilde{L} = 5M$ ,  $a = 0.5M$ ,  $\tilde{q}B_0 = 2M^{-1}$  and  $\tilde{q}\tilde{Q} = 2$  with the initial condition  $r(0) = 2.9M$ ,  $\theta(0) = 0.856$  and  $u^r(0) = 0$ .

ination of the binary values that are constructed from the trajectory  $\mathbf{x}(t)$ . Results of the orbit analysis can be quantified statistically in terms of the Recurrence Quantification Analysis (RQA).<sup>2</sup>

The RP construction is straightforward regardless of the dimension of the phase space. We only need to evaluate the binary values of the recurrence matrix  $\mathbf{R}_{ij}$ , which can be formally expressed as follows:

$$\mathbf{R}_{ij}(\varepsilon) = \Theta(\varepsilon - \|\mathbf{x}(i) - \mathbf{x}(j)\|), \quad i, j = 1, \dots, N, \quad (10)$$

where  $\varepsilon$  is a pre-defined threshold parameter,  $\Theta$  the Heaviside step function, and  $N$  specifies the sampling frequency. The sampling frequency is applied to the time segment of the trajectory  $\mathbf{x}(t)$  under examination. There is, however, no unique prescription for the appropriate definition of the phase space norm  $\|\cdot\|$  in eq. (10). We can consider a purely abstract vector space and apply one of the elementary norms  $L^1$ ,  $L^2$  (Euclidean norm) or  $L^\infty$  (maximum norm). Some aspects of the appropriate choice of the norm are deferred to Appendix A.

Finally, we need to specify the value of the threshold parameter  $\varepsilon$ . To this end we follow the suggestion of Marwan et al. (2007, sec. 3.2.2) and relate  $\varepsilon$  to the standard mean deviation,  $\sigma$ , of the given data set. Setting  $\varepsilon = k\sigma$  is advantageous because the proportionality constant  $k$ , once adjusted to obtain a properly filled Recurrence Plot, remains valid (with only minor adjustments) for all data sets of other trajectories. We therefore normalize the time series of each coordinate separately to zero mean and  $\sigma = 1$ .

The binary valued matrix  $\mathbf{R}_{ij}$  represents the RP which we get by assigning a black dot where  $\mathbf{R}_{ij} = 1$  and leaving a white dot where  $\mathbf{R}_{ij} = 0$ . Both axes represent a time segments over which the data set (the phase space vector) is being examined. RP is thus symmetric; the main diagonal is always occupied by the line of identity

(LOI).

Recurrence Plots contain wealth of information about the dynamics of the system (Thiel et al. 2004a). Different pieces of knowledge are encoded in large-scale and short-scale patterns (Marwan et al. 2007, sec. 3.2.3). To decide if a particular trajectory is a regular or a chaotic one, the determining factor is the presence of diagonal structures in the RP. Diagonal lines in the RP reflect the time segments of phase space trajectory during which the system evolution proceeds in a regular way. It captures the epoch when the trajectory proceeds almost parallel to its previous segment, i.e. within the  $\varepsilon$ -tube around that segment. Hence, integrable systems exhibit themselves by diagonally oriented structures in their RP. On the other hand, if the motion is chaotic the diagonal lines disappear and the diagonal features become shorter, as the trajectories tend to diverge quickly. As a result, more complicated structures appear in the RP.

We stress that the interpretation of the RP is primarily intuitive. We refer to the review paper Marwan et al. (2007, sec. 3.2.3) where the patterns appearing in the RP and their relation to the current dynamic regime are analyzed in detail. Although basic conclusions may be inferred in general (e.g. distinction between regular versus chaotic regime) the fine structure of the RP depends heavily on the properties of a given dynamic system. In order to gain more insight into the way in which various dynamical regimes manifest themselves in our system we typically present RPs accompanied by corresponding Poincaré surface of section throughout this paper.

Visual behavior of RP and its complexity is quantitatively reflected in RQA. The RQA evaluates statistical characteristics of the recurrence matrix  $\mathbf{R}_{ij}$ . First of all, we define the recurrence rate (RR) as a density of points in RP,

$$\text{RR}(\varepsilon) \equiv \frac{1}{N^2} \sum_{i,j=1}^N \mathbf{R}_{i,j}(\varepsilon). \quad (11)$$

<sup>2</sup> We use the CRP ToolBox (Marwan et al. 2007, p. 321) in Matlab (R2009b) to construct RPs and to evaluate RQA measures.

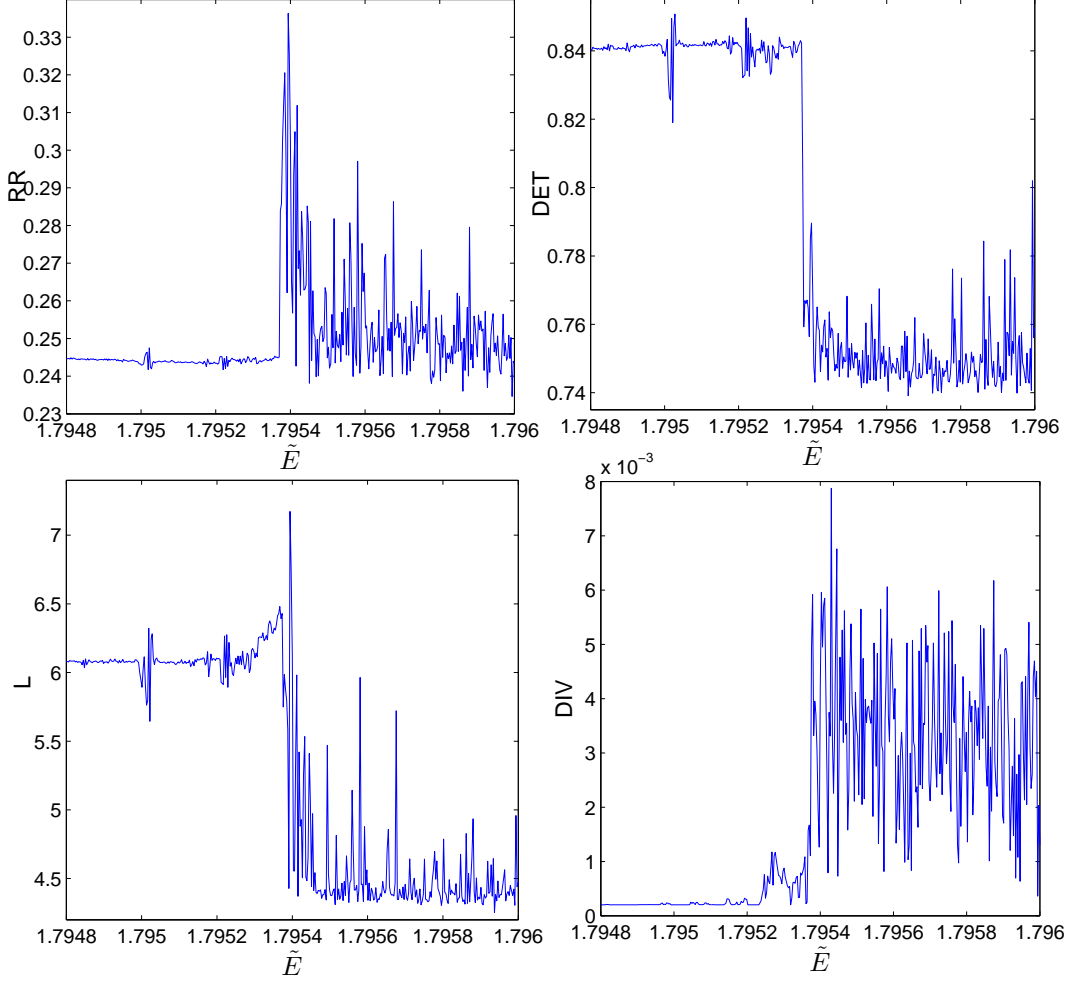


**Figure 8.** Graphs of different RQA measures based on the diagonal lines in the RP as a function of specific energy  $\tilde{E}$ . In each panel, 400 trajectories were analyzed in a given energetic range. All measures exhibit the evident change of their behavior at  $\tilde{E} \approx 1.7954$  which we interpret as an onset of chaos. Other parameters remain fixed at following values:  $\tilde{L} = 5M$ ,  $\tilde{q}B_0 = 2$ ,  $r(0) = 2.9M$ ,  $\theta(0) = 0.856$ ,  $u^r(0) = 0$ ,  $a = 0.5M$  and  $\tilde{q}\tilde{Q} = 2$ .

Now we can turn our attention to diagonal segments in RP. Their length draws distinction between regularity and chaos. The histogram  $P(\varepsilon, l)$  records the number of diagonal lines of length  $l$ . It is formally given as follows:

$$P(\varepsilon, l) = \sum_{i,j=1}^N (1 - \mathbf{R}_{i-1,j-1}(\varepsilon))(1 - \mathbf{R}_{i+l,j+l}(\varepsilon)) \quad (12)$$

$$\times \prod_{k=0}^{l-1} \mathbf{R}_{i+k,j+k}(\varepsilon).$$

This histogram defines the determinism factor (DET), defined as a fraction of recurrence points, which form the diagonal lines of length at least  $l_{\min}$  to all recurrence points,

$$\text{DET} \equiv \frac{\sum_{l=l_{\min}}^{L_{\max}} lP(\varepsilon, l)}{\sum_{l=1}^{L_{\max}} lP(\varepsilon, l)}. \quad (13)$$

The average length of diagonal lines  $L$  (where only lines of length at least  $l_{\min}$  count) is

$$L \equiv \frac{\sum_{l=l_{\min}}^{L_{\max}} lP(\varepsilon, l)}{\sum_{l=l_{\min}}^{L_{\max}} P(\varepsilon, l)}, \quad (14)$$

and the corresponding divergence (DIV) is defined as inverse of the length of the longest diagonal line  $L_{\max}$ ,

$$\text{DIV} \equiv \frac{1}{L_{\max}}. \quad (15)$$

DIV is in its very nature closely related to the divergent features of the phase space trajectory, and so it was originally (Eckmann et al. 1987) claimed to be directly related to the largest positive Lyapunov characteristic exponent  $\lambda_{\max}$ . On the other hand, theoretical considerations justify the use of DIV as an estimator only for the lower limit of the sum of the positive Lyapunov exponents (Marwan et al. 2007, sec. 3.6). Nevertheless, a strong correlation between DIV and  $\lambda_{\max}$  arises in numerical experiments (Trulla et al. 1996).

The quantification measure ENTR is defined as the Shannon entropy of the probability  $p(\varepsilon, l) = P(\varepsilon, l)/N_l$  of finding a diagonal line of length  $l$  in the Recurrence Plot,

$$\text{ENTR} \equiv - \sum_{l=l_{\min}}^{L_{\max}} p(\varepsilon, l) \ln p(\varepsilon, l), \quad (16)$$

where  $N_l$  is a total number of diagonal lines:  $N_l(\varepsilon) =$

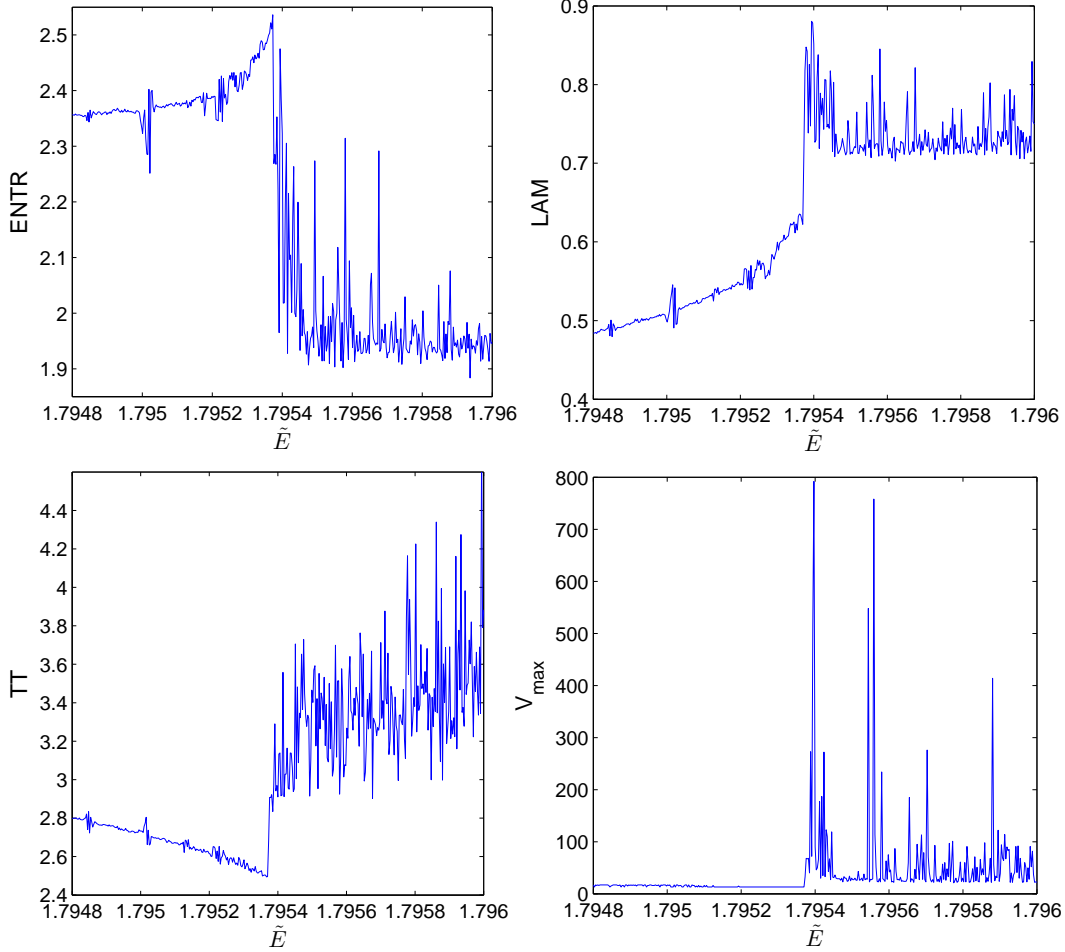


**Figure 9.** Shannon entropy of probability distribution of diagonal lines lengths ENTR and three RQA measures based on the vertical lines of RPs as a function of specific energy  $\tilde{E}$  (details in the text). To some surprise, the vertical measures also react dramatically to the onset of chaos at  $\tilde{E} = 1.7954$ .

$$\sum_{l \geq l_{\min}} P(\varepsilon, l).$$

Analogous statistics may be performed for vertical as well as the horizontal segments (RP is symmetric with respect to the main diagonal). These segments are generally connected with periods in which the system evolves during its laminar state. To this end, the histogram  $P(\varepsilon, v)$  records the number of vertical lines of length  $v$  and it can be constructed as follows:

$$P(\varepsilon, v) = \sum_{i,j=1}^N (1 - \mathbf{R}_{i,j}(\varepsilon))(1 - \mathbf{R}_{i,j+v}(\varepsilon)) \prod_{k=0}^{v-1} \mathbf{R}_{i,j+k}(\varepsilon). \quad (17)$$

In analogy with the diagonal statistics histogram,  $P(\varepsilon, v)$  is used to define the vertical RQA measures. Laminarity (LAM) is defined as a fraction of recurrence points that form vertical lines of length at least  $v_{\min}$  to all recurrence points,

$$\text{LAM} \equiv \frac{\sum_{v=v_{\min}}^{V_{\max}} v P(\varepsilon, v)}{\sum_{v=1}^{V_{\max}} v P(\varepsilon, v)}. \quad (18)$$

The trapping time (TT) is an average length of vertical lines,

$$\text{TT} \equiv \frac{\sum_{v=v_{\min}}^{V_{\max}} v P(\varepsilon, v)}{\sum_{v=v_{\min}}^{V_{\max}} P(\varepsilon, v)}. \quad (19)$$

Finally, the length of the longest vertical line ( $V_{\max}$ ) can also be of some interest.

RQA measures the crucial dependence of RP on the value of the threshold parameter,  $\varepsilon$ , which must be adjusted appropriately to a given data set. This lack of invariance is a drawback of both RPs and RQA. Nevertheless, it was shown (Thiel et al. 2004b) that stable estimates of various dynamical invariants, such as the second order Rényi entropy and the correlation dimension, can be inferred if  $\varepsilon$  is kept within a reasonable range. Since we shall use the standard RQA measures to compare the dynamics between test particles with different initial conditions, we have to eliminate the numerical effect of variations in the range of coordinate values spanned by these trajectories. We achieve this by fixing the value of  $\varepsilon$ .

After the brief set of preliminaries we are now prepared to proceed to the intended application of the recurrence analysis in the next section.

#### 4. KERR BLACK HOLE IN UNIFORM MAGNETIC FIELD

Large-scale magnetic fields are known to be present in cosmic conditions. They can exist around black holes, which do not support their own magnetic field but may be embedded in fields of distant sources. In the case of neutron stars, dipole-type magnetic fields of very high strength often arise. We concentrate on black holes in this section and defer the case of a magnetic star to sec.



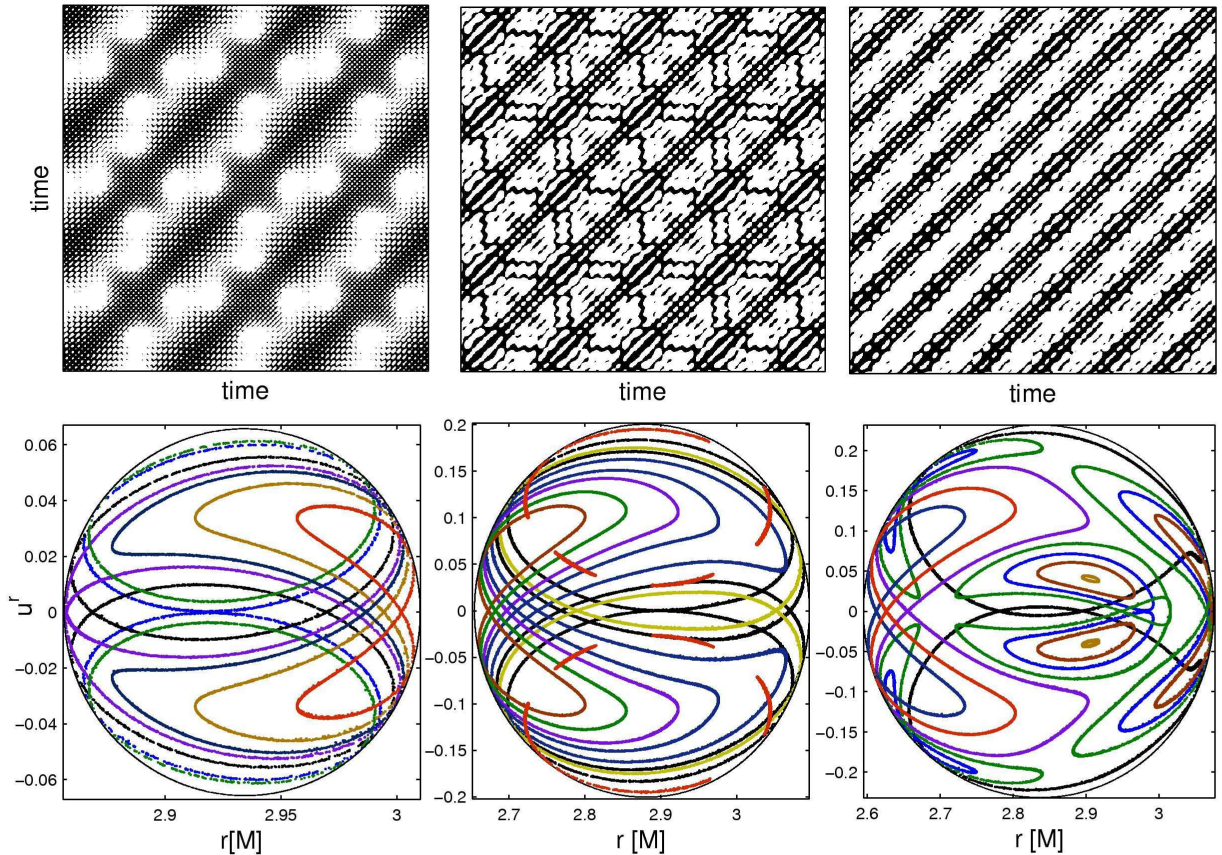


**Figure 10.** Comparison of purely off-equatorial trajectories in spacetimes differing by the spin parameter  $a$  (left panels:  $a = 0.3M$ ; middle:  $a = 0.6M$ ; right:  $a = M$ ) which is linearly linked to the energy  $\tilde{E}$  (left panels:  $\tilde{E} = 1.56$ ; middle:  $\tilde{E} = 1.9$ , and  $\tilde{E} = 2.35$  in the right panels). Other parameters remain fixed:  $\tilde{L} = 5M$ ,  $M^{-1}$ ,  $\theta(0) = \theta_{\text{section}} = 0.856$ ,  $\tilde{q}B_0 = 2M^{-1}$  and  $\tilde{q}\tilde{Q} = 2$ . RPs are taken for trajectories with  $r(0) = 2.9M$  and  $u^r(0) = 0$ . Although the structures in the Recurrence Plots clearly differ from each other, all of them represent diagonally oriented patterns that are characteristic of regular motion. The regularity of the motion is confirmed by surfaces of section in the bottom panels, where several trajectories (for each value of spin and energy) are presented. Different colours (grey scaled in the printed version of the paper) are used to distinguish the orbits originating from different initial conditions.

5.

By employing the uniform test field solution (Wald 1974) we incorporate a weak large-scale magnetic field near a rotating black hole. The vector potential can be expressed in terms of Kerr metric coefficients (9) as follows,

$$A_t = \frac{1}{2}B_0(g_{t\phi} + 2a g_{tt}) - \frac{1}{2}\tilde{Q}g_{tt} - \frac{1}{2}\tilde{Q}, \quad (20)$$

$$A_\phi = \frac{1}{2}B_0(g_{\phi\phi} + 2a g_{t\phi}) - \frac{1}{2}\tilde{Q}g_{t\phi}, \quad (21)$$

where  $B_0$  is magnetic intensity and  $\tilde{Q}$  stands for the test charge on the background of Kerr metric. The terms containing  $\tilde{Q}$  can be identified with the components of the vector potential of Kerr-Newman solution (although the test charge does not enter the metric itself). An example of an integrated trajectory is shown in Fig. 1. Wald (1974) has shown that the black hole selectively accretes charges from its vicinity, until it becomes itself charged to the equilibrium value

$$\tilde{Q}_W = 2B_0a. \quad (22)$$

We remark that the particle charge  $\tilde{q}$  appears always as a product with  $\tilde{Q}$  or  $B_0$  in the formula (5) for the effective potential, as well as in equations of motion (2). Therefore, the simultaneous alteration of  $\tilde{q}$ ,  $\tilde{Q}$  and  $B_0$

values, preserving the products  $\tilde{q}\tilde{Q}$  and  $\tilde{q}B_0$ , does not affect the particle dynamics. If we further assume that  $\tilde{Q} = \tilde{Q}_W = 2B_0a$  is maintained, we only need to specify the value of  $\tilde{q}B_0$  to uniquely determine a particular trajectory. However, since we do not restrict ourselves to the case  $\tilde{Q} = \tilde{Q}_W$  we decide to always explicitly specify the values of  $\tilde{q}\tilde{Q}$  and  $\tilde{q}B_0$ .

#### 4.1. Motion within the potential lobes

Our previous analysis (Kovář et al. 2010) concludes that the off-equatorial bound orbits are allowed only for test particles obeying simultaneously the two conditions,  $\text{sgn}(aL) = 1$  and  $\text{sgn}(\tilde{q}) = \text{sgn}(aB_0)$ . Three distinct types were found (see Fig. 2) and we examined the dynamics of test particles in all of these types. The results for different types are comparable, and so we present here only the analysis of one of them, namely the type Ia. While raising the energy level from the local minima of the symmetric halo orbits, we observe that the off-equatorial lobes grow and eventually merge with each other once the energy of the saddle point in the equatorial plane is reached.

The size of the lobes is controlled by the specific energy  $\tilde{E}$ . Employing the Poincaré surfaces of section and the Recurrence Plots we investigate how the regime of the particle motion changes with  $\tilde{E}$ . This parameter appears

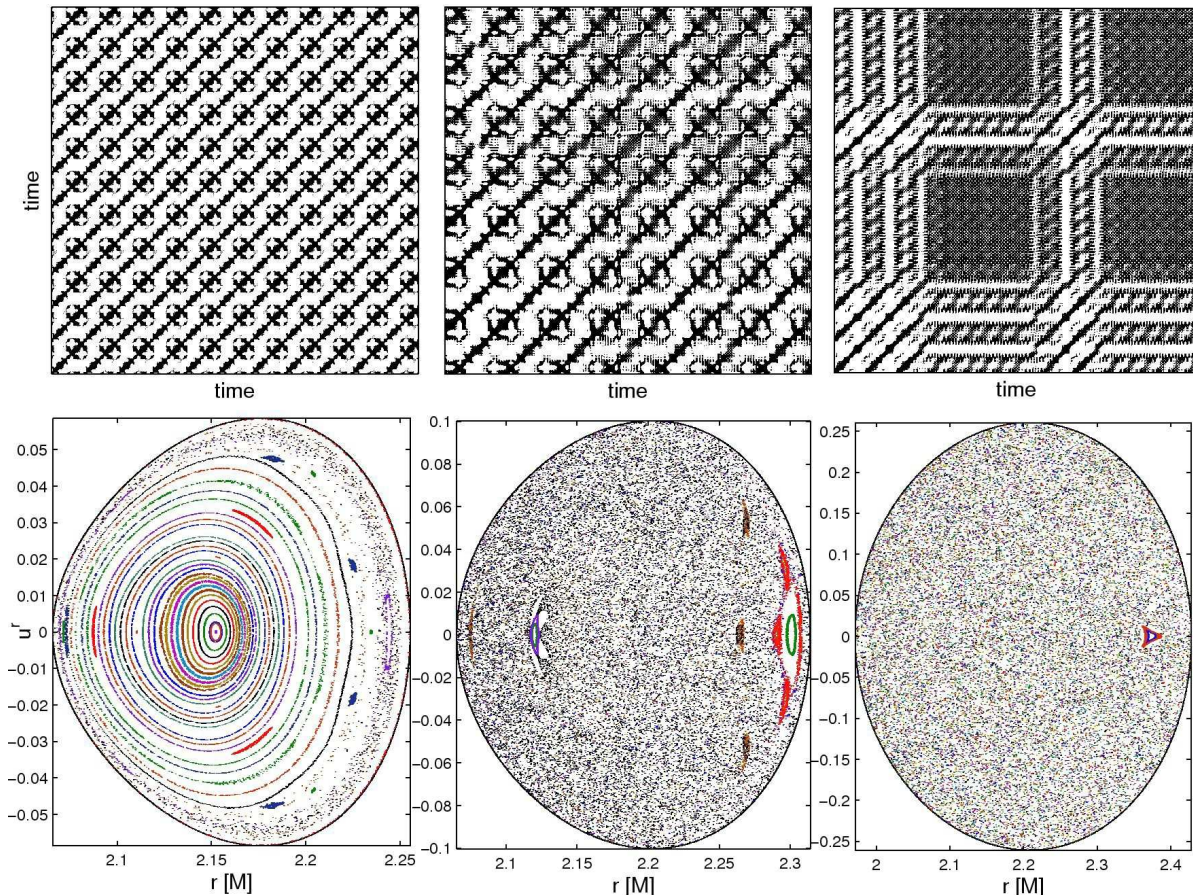


**Figure 11.** Comparison of trajectories of particles launched from the equatorial plane with different spin values. Also in this case we have to link linearly the value of spin  $a$  with  $\tilde{E}$  in order to maintain the existence of the potential lobe. In left panels we set  $a = 0.5M$ ,  $\tilde{E} = 1.795$ , in middle panels  $a = 0.6M$ ,  $\tilde{E} = 1.92$  and in right panels  $a = M$ ,  $\tilde{E} = 2.42$ . For all three cases we show surfaces of section of several trajectories differing in initial values  $r(0)$  and  $u^r(0)$ . Recurrence Plots are taken for trajectories with  $r(0) = 2.15M$ ,  $u^r(0) = 0$ . Other parameters remain fixed:  $\tilde{L} = 5M$ ,  $\tilde{q}B_0 = 2M^{-1}$ ,  $\theta(0) = \theta_{\text{section}} = \frac{\pi}{2}$ ,  $\tilde{q}\tilde{Q} = 2$ .

as a suitable control parameter producing a sequence of bound trajectories while all other parameters (and the initial position) remain fixed. For the sake of comparison we first present the case of a fully integrable system of a charged test particle on the pure Kerr-Newman spacetime (Fig. 3). The motion occurs in the potential lobe around the local minimum in the equatorial plane; there are no halo orbits above the horizon in this case (Kovář et al. 2010; de Felice 1979).

Figure 4 shows regular motion occurring in the off-equatorial lobe on the Kerr background with Wald test field. Increasing the energy level (while keeping all other parameters fixed) above the value in the equatorial saddle point results in a transitional regime depicted in Fig. 5. The onset of chaotic features does not occur as a direct consequence of the lobe merging. We rather observe that the orbit bound in merged (cross-equatorial) lobe remains regular until the particle *notices* the possibility of crossing the equatorial plane which happens when its energy is increased sufficiently. Once the motion becomes cross-equatorial, chaotic features appear. By increasing the energy even more we approach the critical value when the lobe opens and allows the particles to fall onto the horizon. For energies slightly below this limit we detect a fully chaotic regime of motion (Fig. 6).

Figure 7 shows an alternative representation of the re-

currence plots, where the distance to the nearest neighboring point along the phase space trajectory is encoded by different colors. Again, by comparing the two panels one can clearly recognize how the diagonal structures disintegrate into scattered points as the chaos sets in.

From the survey of Poincaré surfaces of section and the Recurrence Plots we may only conclude that the transition from the regular to chaotic regime occurs somewhere close to the value  $\tilde{E} = 1.796$ . In order to localize this transition more precisely we evaluate RQA measures for 400 trajectories with the energy spread equidistantly over the interval  $\tilde{E} \in (1.7948, 1.7968)$ . In figs. (8) and (9), we observe a sudden change of the behavior of the statistical measure at  $\tilde{E} \approx 1.7954$ , reflecting a dramatic change of the particle dynamics.

Moreover, we know that the divergence DIV is related to the Lyapunov exponents, and in Fig. 8 we observe that it suddenly rises at  $\tilde{E} \approx 1.7954$ , meaning that the trajectories become more divergent when this energy is reached. All of these indications combined lead to the conclusion that this energy level represents a critical value at which a transition from regular to chaotic regime occurs.

We conclude that the energy of the particle  $\tilde{E}$  acts as a governing factor determining the dynamic regime of motion. Our survey across various initial conditions

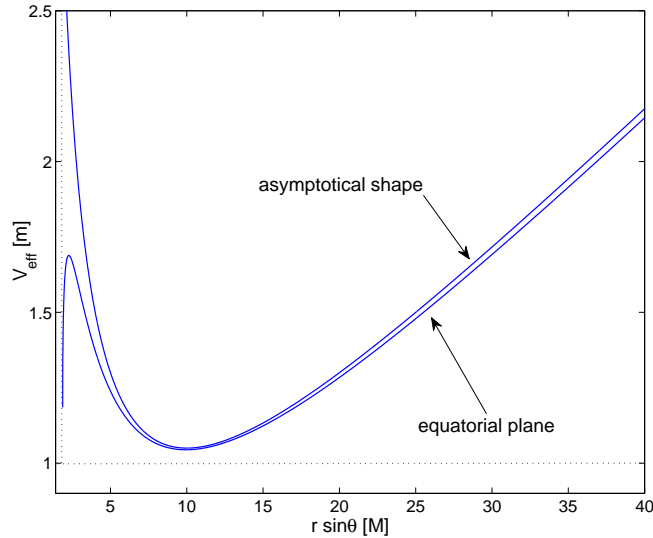


**Figure 12.** Profiles of the effective potential  $V_{\text{eff}}$  for  $\tilde{L} = 5M$ ,  $a = 0.5M$ ,  $\tilde{q}\tilde{Q} = 1.03$ ,  $\tilde{q}B_0 = 0.1M^{-1}$ , taken in the equatorial plane and in the asymptotic region  $z = r \cos \theta \rightarrow \infty$  (as indicated with the corresponding curves). The valley crosses the equatorial plane, almost unaffected in its bottom parts, although the behavior of the potential near the symmetry axis is quite different in the equatorial plane where it approaches the horizon of the black hole (vertical dotted line at  $r = r_+(a)$ ). The horizontal dotted line at unity measures the rest energy of the particle  $m$ .

has shown that motion in potential wells of the type Ia in a Wald test field is generally regular. Chaos appears well after the merging point of the lobes and close to the critical breaking energy. We have verified that all queried RQA measures, i.e. not only those based on diagonal lines in RP, react to the transition from the regular to chaotic regime of motion, allowing us to localize precisely the transition. This was fully confirmed also in the other two types (classes Ib and Ic of our typology in Fig. 2).

#### 4.2. The effect of spin on the chaoticness of motion

Much attention has been recently focused towards the problem of determining the black hole spin from the properties of motion of surrounding matter (Narayan 2005; Reynolds & Nowak 2003). The astrophysical motivation to address these issues arises from the fact that cosmic black holes are fully described by three parameters – mass, electric charge and spin. While the methods of mass determination have been widely discussed (e.g. Casares 2007; Vestergaard 2010; Czerny & Nikolajuk 2010), the electric charge is considered to be negligible because of rapid neutralization of black holes via selective accretion. However, determining the spin is a much more challenging task: the spin is important, but its influence is apparent only *very* near the black hole horizon (Murphy et al. 2009).

One can raise a question of whether the value of spin parameter  $a$  of the Kerr black hole affects the dynamical regime of motion in the immediate neighborhood of the black hole. In other words, we ask if the spin parameter  $a$  triggers or diminishes the chaoticness of the system. Answering this question is not straightforward because by altering the spin across an interval of values ( $a^2 \leq M^2$ ) we inevitably have to change some other variables of the system; otherwise the different cases could not be directly compared. Moreover, the location and the very existence of the potential lobes is not automatically ensured over the whole range of spin because of strong  $V_{\text{eff}}(a)$  dependence.

We found that in order to keep the off-equatorial lobe

at the initial position and the original size we need to increase the energy  $\tilde{E}$ , roughly proportionally to the increment of  $a$ . The effect of increasing  $a$  exhibits itself by lifting the hyperplane of effective potential. To compensate for this effect we have to elevate the  $\tilde{E}$ -plane at which we cut the potential, so that we obtain (roughly) the original closed contour (the potential lobe) inside of which the motion is confined. It turns out that this can be achieved by linking both quantities linearly.

First we compare the dynamics in the off-equatorial lobe in the range  $\frac{a}{M} \in (0.3, 1)$  (for  $a \lesssim 0.3M$  the topology of the effective potential changes) to which we linearly relate the energy range  $\tilde{E} \in (1.56, 2.35)$  (whilst other parameters are kept fixed as follows:  $\tilde{L} = 5M$ ,  $\tilde{q}B_0 = 2M^{-1}$ ,  $r(0) = 2.9M$ ,  $\theta(0) = 0.856$ ,  $u^r(0) = 0$ ,  $\tilde{q}\tilde{Q} = 2$ ). By inspecting the Poincaré surfaces of section and performing the recurrence analysis for a large number of trajectories across the given range of  $a$  and  $\tilde{E}$  (exemplary cases presented in Fig. 10) we come to the conclusion that there is no overall trend that could suggest that  $a$  is the unique driving agent affecting the regime of motion. All trajectories in our survey exhibit a regular behavior, which is also in agreement with the previous conclusion that the motion in off-equatorial potential lobes associated with the Wald test field is generally regular.

We also examined the dynamics of test particles launched from the equatorial plane whose trajectories occupy the potential lobe extending symmetrically above and below the equatorial plane. A given lobe maintains its size for spin values  $\frac{a}{M} \in (0.5, 1)$  and the related interval of energy  $\tilde{E} \in (1.795, 2.42)$ . A survey across the given range of spin (energy) values reveals for this class of trajectories both chaotic and regular regimes. In Fig. 11 we observe that for the lowest inspected spin,  $a = 0.5M$  ( $\tilde{E} = 1.795$ ), the regular motion dominates, although islands of chaotic behavior are also present. Increasing the spin (energy) we observe that regular trajectories grad-

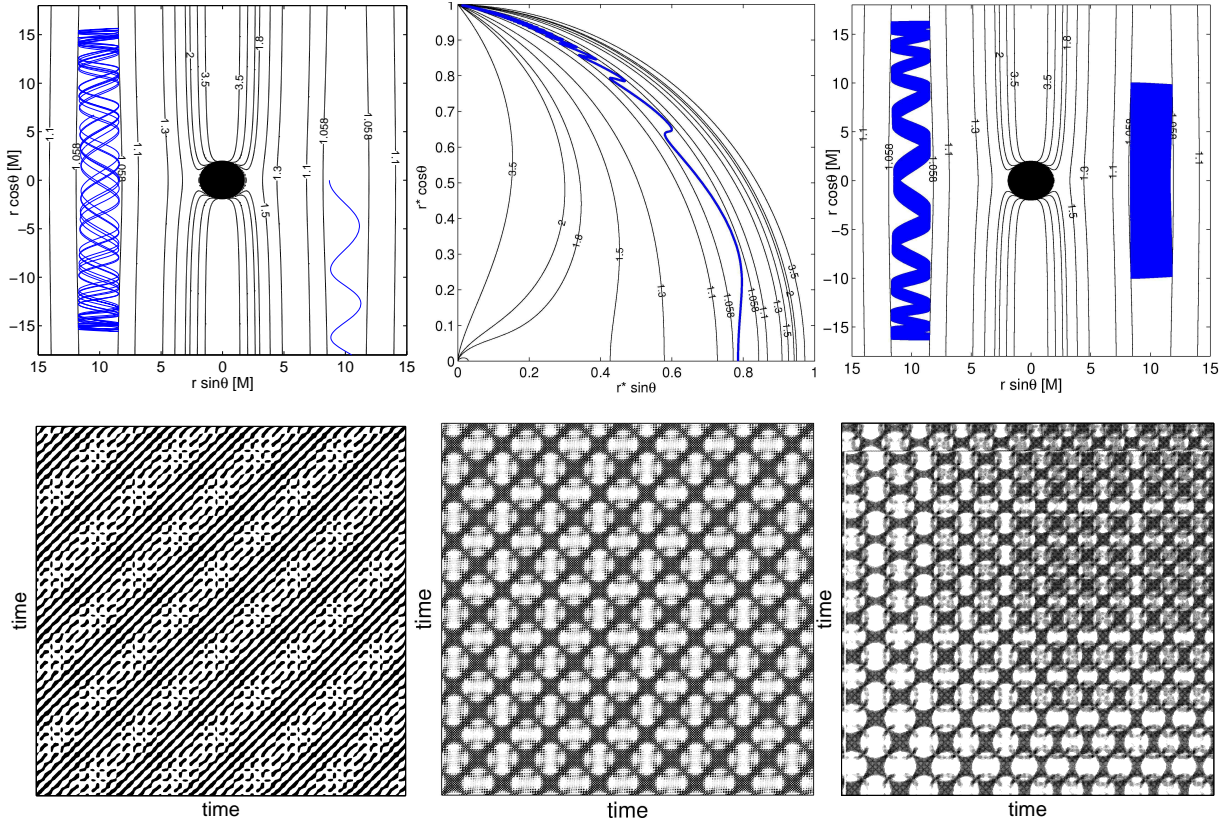


**Figure 13.** An exemplary trajectory ( $\tilde{E} = 1.058$ ,  $\tilde{L} = 5M$ ) is launched from the equatorial plane  $\theta(0) = \frac{\pi}{2}$  with  $u^r(0) = 0$ . Parameters of the background are  $a = 0.5M$ ,  $\tilde{q}B_0 = 0.1M^{-1}$ ,  $\tilde{q}\tilde{Q} = 1.03$ . In the upper left panel we observe that setting  $r(0) = 8.4M$  results in oscillations around the equatorial plane while launching it at  $r(0) = 8.7M$  makes it escape. In the upper middle panel we examine the trajectory of the escaping particle in terms of the rescaled radial coordinate  $r^* \equiv \frac{r-r_+}{r_-}$ . In the case of oscillating trajectories two distinct modes of motion are observed (upper right panel). The first particle ( $r(0) = 11.5M$ ) shows a complex “ribbon-like” trajectory; the other one ( $r(0) = 8.4M$ ) fills uniformly the given portion of the potential valley. The Recurrence Plots are also shown (bottom panels). We observe a highly ordered regular pattern for the particle with  $r(0) = 8.4M$  (left panel), a more complicated diagonal pattern of the ribbon-like trajectory (launched at  $r(0) = 11.5M$ , middle panel), and a disrupted diagonal pattern of the transitional trajectory ( $r(0) = 11.4M$ , right panel).

ually diminish. For  $a = 0.6M$  ( $\tilde{E} = 1.92$ ) some regular orbits still appear, but they are already dominated by chaotic trajectories. For higher spins the traces of regular motion further diminish. We present the extreme case  $a = M$  ( $\tilde{E} = 2.42$ ) in Fig. 11 to illustrate this apparent chaotic takeover.

We conclude that for the class of orbits originating in the equatorial plane, spin  $a$  could possibly act as a destabilization factor which triggers the chaotic motion if enhanced sufficiently. However since the energy  $\tilde{E}$  is increased simultaneously it is not possible to attribute the observed dependence to the spin *itself*. On the other hand we have already seen in the above-given discussion (sec. 4.1) that energy  $\tilde{E}$  may *itself* act as a key factor determining the dynamic regime of motion. Thus we suggest to attribute the observed triggering of the chaos to the increase of energy  $\tilde{E}$  rather than spin  $a$ .

We remark that a similar problem concerning the spin dependence of the motion chaoticness was addressed recently by Takahashi & Koyama (2009). Authors of the quoted paper employ a dipole magnetic test field upon a Kerr background and perform a study of test particle trajectories, concluding that increasing the value of the spin parameter stabilizes the motion in a given setup. Unlike our case, the topology of the effective potential in their scenario allows the chosen potential lobe to be

maintained at a given location and roughly the same size (but not the same depth) even if  $a$  varies while  $\tilde{E}$  is kept constant. However increasing the spin allows the authors to set gradually lower and lower energies, for which more regular trajectories are found. This is not at all surprising in perspective of our results, where the energy  $\tilde{E}$  proved to play a key role in determining the stability of motion. Although a direct comparison of presented surfaces of section differing only in  $a$  value may suggest the spin dependence, there is no clear and unambiguous correlation. We thus suggest attributing the observed dependence primarily to the level of energy, which acted as a motion destabilizer also in our setup. In fact, even if a real trend with the spin is present, it is hard to disentangle it from a simultaneous change of  $\tilde{E}$ .

The question of the dependence of the dynamics upon the other parameters of the system ( $\tilde{L}$ ,  $\tilde{q}B_0$ ,  $\tilde{q}\tilde{Q}$ ) was also addressed during the analysis. It appeared that above mentioned difficulties accompanying the analysis of the spin dependence became even more serious in this case. Namely, neither it was possible to maintain the given potential lobe for a reasonable range of values of selected parameter nor we were able to fix this problem by binding this parameter in some simple manner to some other parameter (e.g. energy  $\tilde{E}$ ). In other words, none of these parameters itself may be regarded as a trigger for chaos.

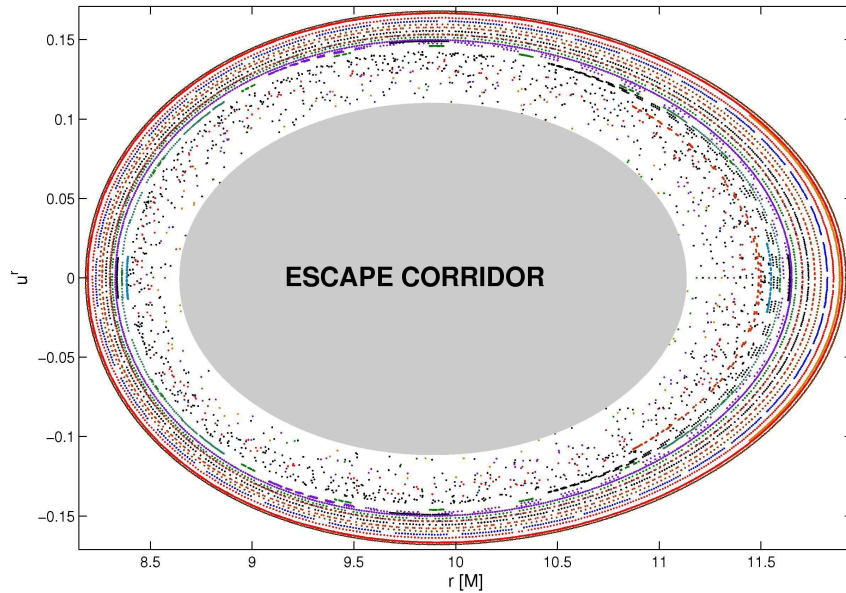


**Figure 14.** The Poincaré surface of section of several trajectories ( $\tilde{E} = 1.058$ ,  $\tilde{L} = 5M$ ,  $\tilde{q}B_0 = 0.1M^{-1}$ ,  $\tilde{q}\tilde{Q} = 1.03$ ,  $a = 0.5M$ ,  $\theta = \frac{\pi}{2}$ ) launched from the equatorial plane with various values of  $r(0)$  and  $u^r(0) = 0$ . Grey colour indicates the escape corridor which lets the particles escape from the equatorial plane (see details in the text).

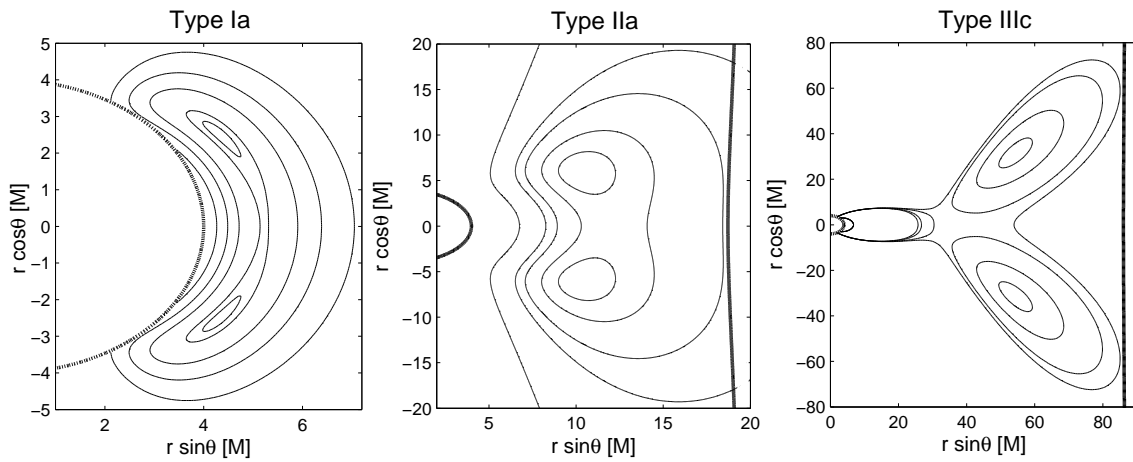


**Figure 15.** Selected types of the effective potential behavior in the vicinity of off-equatorial halo orbits above the surface of magnetic star with rotating dipole magnetic field. The inner bold line signifies the surface of the star at  $r = 4M$ . The outer line is the light surface.

#### 4.3. Motion in potential valleys

Besides off-equatorial lobes, the potential may form another remarkable structure – an endless potential valley of almost constant depth which runs parallelly to the symmetry axis (Fig. 12). The poloidal orientation and asymptotical form of the valley are due to the fact that the Wald test field does not vanish at spatial infinity and it approaches the uniform magnetic field parallel to the symmetry axis.

The existence of such a potential corridor suggests that test particles with a particular range of parameter values could escape from the equatorial plane to large distance. We observe that a test particle in the potential valley can keep oscillating around the equatorial plane or it may escape from this plane completely, depending on its initial position in the phase space (see the upper left panel of Fig. 13). We can examine the motion in the asymptotic region by rescaling the radial coordinate (upper middle panel of Fig. 13). To achieve this, we use  $r^* \equiv \frac{r-r_+}{r}$ ,

where  $r_+ = M + \sqrt{M^2 - a^2}$  is the position of the outer horizon of the black hole.

The normalization condition allows one to express  $u^\theta$  as a function of other phase space variables and parameters of the system. Intuition suggests that, considering particles launched from the equatorial plane ( $\theta(0) = \frac{\pi}{2}$ ), the initial value  $u^\theta(0)$  is a governing parameter which decides whether the particle remains oscillating around  $\theta = \frac{\pi}{2}$  or leaves it once forever. We can draw the isolines of selected  $u^\theta$  values in the  $(r, u^r)$ -plane which we use as a surface of section ( $\theta_{\text{section}} = \frac{\pi}{2}$ ) for the inspection of the test particle dynamics. Comparing acquired isolines for various values of  $u^\theta$  with the empirically stated escape corridor of Fig. 14 leads to the conclusion that they never coincide perfectly, although the correlation is quite high. In other words there is no definite threshold value of  $u^\theta(0)$  which would determine whether a selected combination of  $r(0)$ ,  $u^r(0)$  (while other parameters are fixed) lets the particle launched at equatorial plane leave

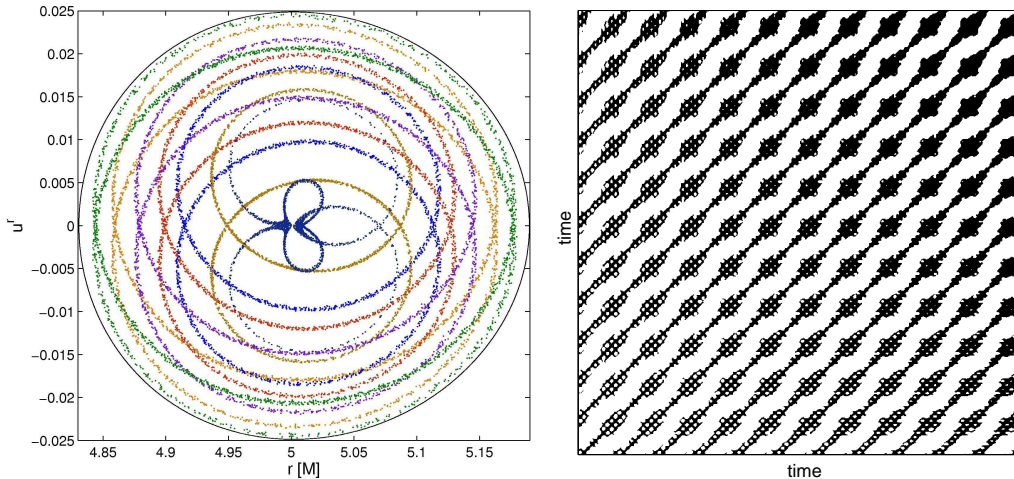


**Figure 16.** Regular motion in the off-equatorial potential lobe at the energy level  $\tilde{E} = 0.8482$ . Parameters of the system are  $\tilde{q}\mathcal{M} = -5.71576 M^2$ ,  $\tilde{L} = 0.87643 M$ ,  $\Omega = 0.011485 M^{-1}$ . The left panel shows sections of several trajectories launched from  $\theta(0) = \theta_{\text{section}} = 1.0492$ . One of them ( $r(0) = 5.02 M$  and  $u^r(0) = 0$ ) is visualized in the Recurrence Plot in the right panel. The motion is regular (RP remains diagonal), however, the density of recurrence points clearly grows during the analyzed period.

or oscillate around the plane.

In Fig. 14 we observe several qualitatively different types of possible particle dynamics. Next to the effective potential contour we find closed and well-defined curves which represent the regular motion. Going further inside we notice that fragmented curves are present. Below them we find progressively more and more blurred patterns, which again signifies the onset of chaos. The inner parts of the potential lobe are occupied by the “escape corridor” where the particles can stream freely from the equatorial plane, as seen in Fig. 13.

The trajectories represented by the closed curves in the surface of section differ profoundly from the disconnected curve orbits. The difference can be seen also in the direct projection onto the poloidal plane (upper right panel of Fig. 13). While the trajectories of the first type gradually fill each particular compact region of given section, the latter forms bundles which curl through the projection plane resembling ribbons that bound regions which are never reached by the particle.

By employing the Recurrence Plots (bottom panels of Fig. 13) we confirm that the dynamics differs significantly in these distinct modes of motion. Not surprisingly we obtain a typical regular pattern in the case of trajectory which forms a closed sharp curve in the surface of section (bottom left panel of Fig. 13). A “ribbon-like” trajectory (fragmented curve in Fig. 14) results in an ordered checkerboard pattern (bottom middle panel), which is known to be typical for periodic and quasi-periodic systems (Marwan et al. 2007). Finally, in the bottom right panel of Fig. 13 we observe that a blurred curve trajectory exhibits slight chaotic behavior in its RP. The diagonal structures are partially disrupted and we notice that diagonal lines become bent as they approach the line of identity.

Authors of the recent paper (Lukes-Gerakopoulos et al. 2010) observed patterns similar to our fragmented curves in Poincaré sections of phase space occupied by geodesic trajectories around slightly perturbed Kerr spacetime described by Manko-Novikov metric. They assume that such fragments can be identified with the Birkhoff islands anticipated by the

Poincaré-Birkhoff theorem. A given chain of Birkhoff islands (i.e. the fragmented curve in the section) originates from the resonant torus of an unperturbed system whose orbits have characteristic frequencies in a given rational ratio. The most prominent chains of islands should belong to the resonances characterized by simple integer ratios  $\frac{1}{2}$ ,  $\frac{2}{3}$  etc. Authors of the cited paper conclude that the presence of the Birkhoff islands might be in principle detected (at least in the context of gravitational radiation emitted by extreme mass ratio inspiraling sources) which would prove the system to be perturbed. However, since the assumption of the weakness of the perturbation is generally not fulfilled in our case, we do not explicitly identify fragmented tori in the surfaces of section with the Birkhoff chains.

The class of escaping trajectories in the Kerr background was recently discussed by Preti (2010). The author suggests that a Wald electromagnetic field employed in this setup could serve as a charge separation mechanism for astrophysical black holes since the sign of the particle charge may determine whether a given particle escapes from the equatorial plane or becomes trapped in cross-equatorial confinement (or falls into the horizon).

## 5. A MAGNETIC STAR

We describe the gravitational field outside a compact star by the Schwarzschild metric,

$$ds^2 = - \left(1 - \frac{2M}{r}\right) dt^2 + \left(1 - \frac{2M}{r}\right)^{-1} dr^2 + r^2(d\theta^2 + \sin^2\theta d\phi^2). \quad (23)$$

The associated magnetic field is modeled as a dipole rotating at angular velocity  $\Omega$  (Sengupta 1995):

$$A_t = -\Omega A_\phi = \frac{3\mathcal{M}\Omega\mathcal{R}\sin^2\theta}{8M^3}, \quad (24)$$

$$A_\phi = -\frac{3\mathcal{M}\mathcal{R}\sin^2\theta}{8M^3}, \quad (25)$$

where

$$\mathcal{R} = 2M^2 + 2Mr + r^2 \log\left(1 - \frac{2M}{r}\right). \quad (26)$$

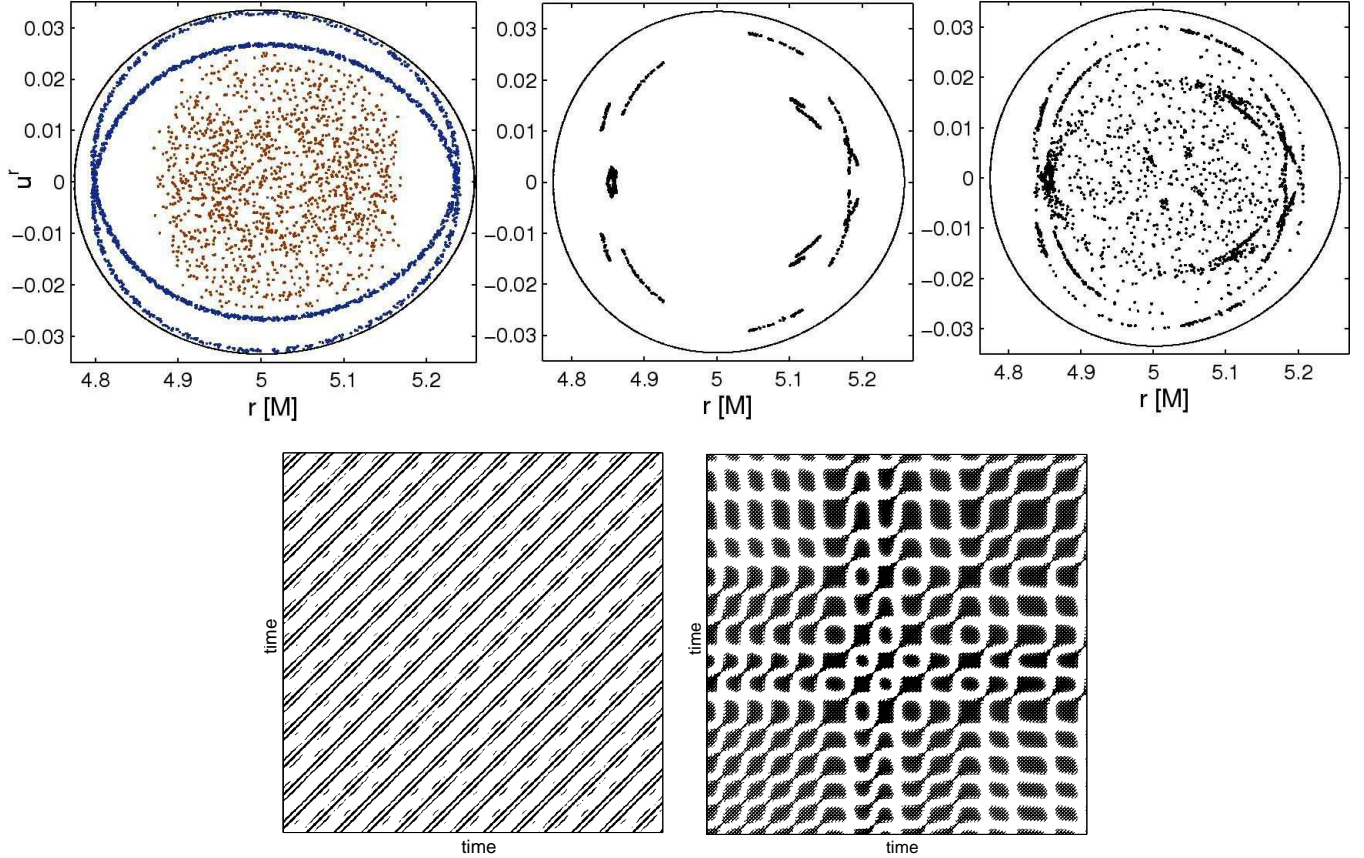


**Figure 17.** For an energy value of  $\tilde{E} = 0.8485$ , both off-equatorial lobes merge via the equatorial plane. The upper-left panel shows Poincaré sections of two trajectories ( $\theta(0) = \theta_{\text{section}} = 1.0492$ ,  $u^r(0) = 0$ ). A particle launched at  $r(0) = 4.8 M$  never crosses the equatorial plane and moves regularly. Setting  $r(0) = 5 M$  we observe a chaotic motion crossing the equatorial plane repeatedly. All particles launched with  $r(0)$ ,  $u^r(0)$ , corresponding to the inner parts of the potential curve, move in the same chaotic manner. The outskirts are occupied by regular trajectories. The upper-middle panel shows the transient trajectory ( $r(0) = 4.85 M$ ), regular during the integration period of  $\lambda = 10^5$ . In the upper-right panel, the integration time is prolonged to  $\lambda = 3 \times 10^5$ . Here, the onset of chaos is connected with the first passage through the equatorial plane. The RP of the regular trajectory with  $r(0) = 4.8 M$  is presented in the bottom-left panel; the RP on the right belongs to the chaotic trajectory with  $r(0) = 5 M$ .

The related dipole moment  $\mathcal{M}$  is given by (Bakala et al. 2010)

$$\mathcal{M} = \frac{4M^3 r_*^{3/2} (r_* - 2M)^{1/2} B_0}{6M(r_* - M) + 3r_* (r_* - 2M) \ln(1 - 2Mr_*^{-1})}, \quad (27)$$

where  $B_0$  is the magnetic field at the neutron star equator,  $r_*$  is the radius of the star surface.<sup>3</sup>

We assume eqs. (23)–(24) to hold outside the star surface ( $r > r_*$ ) and inside the light cylinder ( $u^\mu u_\mu < 0$ ). We set  $r_* = 4M$  as the inner radial boundary of the particle motion. As for the light cylinder, the mentioned condition results in a relation  $r^2 \sin^2 \theta \Omega^2 = 1 - \frac{2M}{r}$ , which implicitly specifies the outer boundary. The vector potential (24) is valid inside the rigidly corotating magnetospheric plasma, which we consider to be an excellent conductor, so that the force-free condition  $F_\nu^\mu u^\nu = 0$  holds for the plasma for which  $u^\mu = (u^t, 0, 0, u^\phi)$  and  $\frac{u^\phi}{u^t} = \Omega$ .

A general formula for the effective potential eq. (5)

<sup>3</sup> The existence of extremely compact stars with  $r_* \approx 3M$  is unlikely, but not excluded (Bahcall et al. 1989; Stuchlík et al. 2009). Most of the realistic equations of state imply a lower limit  $r_* \approx 3.5M$  (Glendenning 1997). On the other hand, the models of Q-stars do allow a lower limit of  $r_* \approx 2.8M$  (Miller et al. 1998).

simplifies to the form

$$V_{\text{eff}} = -\frac{3\tilde{q}\mathcal{M}\mathcal{R}\Omega \sin^2 \theta}{8M^3} + \left(1 - \frac{2M}{r}\right)^{\frac{1}{2}} \left[1 + \left(\frac{\tilde{L}}{r \sin \theta} + \frac{3\tilde{q}\mathcal{M}\mathcal{R} \sin \theta}{8M^3 r}\right)^2\right]^{\frac{1}{2}}. \quad (28)$$

### 5.1. Motion inside the potential lobes

Our previous analysis (Kovář et al. 2010) revealed a number of distinct types of possible topological structures of the effective potential. However it appears that the system is not as rich in its dynamical properties. The test particle trajectories share some similar features across different classes of the effective potential. Therefore, we only present surveys of particle dynamics in three exemplary types: Ia, IIa and IIIc (Fig. 15; see Kovář et al. (2010) for the complete review).

Class Ia lobes grow with energy increasing. Once the level of the equatorial saddle point is reached, the lobes merge with each other across the equatorial plane. The single merged lobe eventually intersects the surface of the star if the energy level is increased sufficiently, letting the particle fall onto the surface. Lobes of IIa type also merge

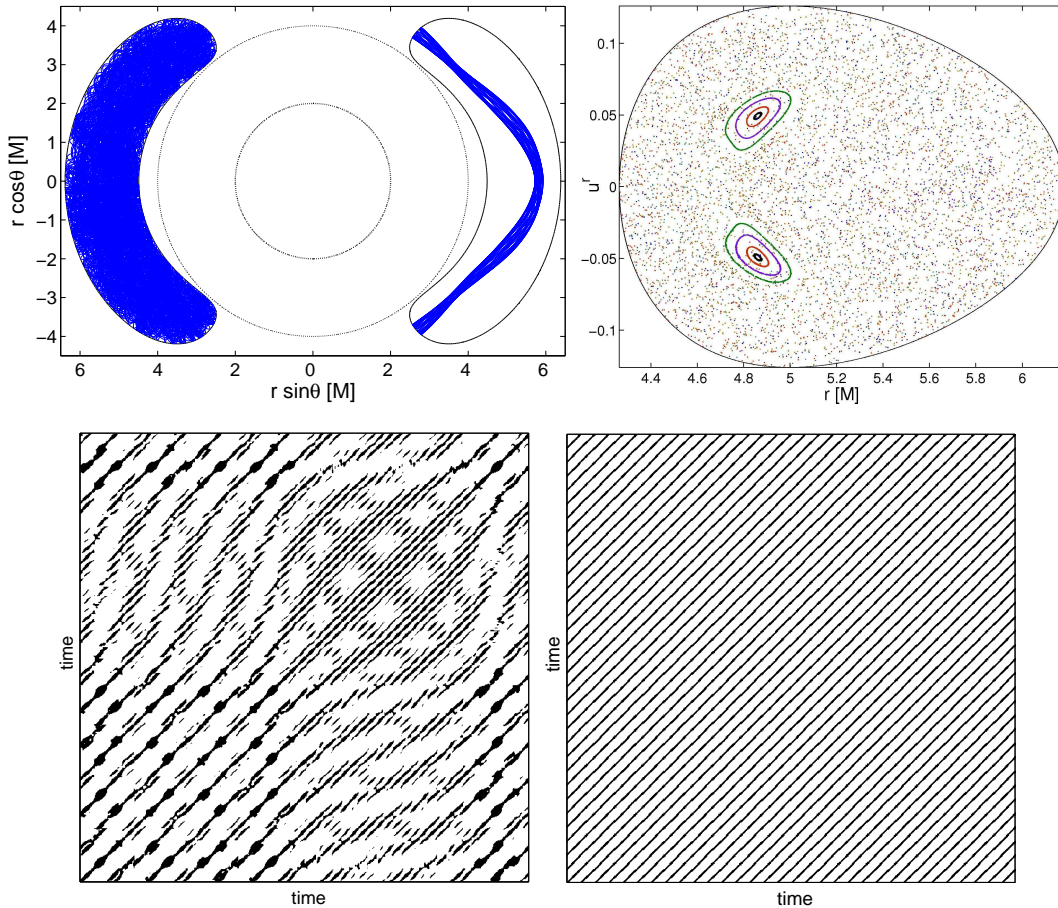


**Figure 18.** For the energy level  $\tilde{E} = 0.857$  we obtain a broad lobe which almost touches the surface of the star at  $r = 4 M$ . In the upper-left panel, we launch two particles with  $\theta(0) = 1.0492$ ,  $r(0) = 4.75 M$ . The particle to the left of the star starts with  $u^r(0) = 0$  and moves chaotically, while the other one with  $u^r(0) = 0.03$  follows a perfectly regular trajectory. The upper right-panel shows these two types of trajectory appear in the surface of section plot. The bottom panels demonstrate the difference between the two types in terms of Recurrence Plots.

via the equatorial plane but in contrast to the first type the merged lobe opens toward the light cylinder (beyond which the model becomes invalid). Lobes of the class IIIc first open via the off-equatorial saddle points, allowing the particles fall onto the star, before the lobes merge through the equatorial plane.

Now we study the three selected types of the effective potential topology in more detail. We are primarily interested whether and how the dynamic regime changes across the given range of specific energy  $\tilde{E}$ . Especially, we shall address what happens with the dynamics when the particle acquires enough energy to cross the saddle point.

The first survey (type Ia) begins at energy level  $\tilde{E} = 0.8482$ , corresponding to the closed lobe. In Fig. 16 we observe that the motion inside the lobe is stable. No chaotic properties are detected – neither in Poincaré surfaces of section nor in the Recurrence Plots.

As the energy increases to  $\tilde{E} = 0.8485$ , the symmetrical lobes merge via the equatorial plane. By inspecting a number of trajectories in this case we find that chaos starts appearing at this point – those particles which notice the gate through the equatorial plane always fill the entire allowed region and they move chaotically. Nevertheless, there are still such particles which move regularly in one of the two parts of merged lobe and never cross

the equatorial plane. We can also find transient trajectories corresponding to regular motion lasting for some period of time in one part of the lobe, followed by chaotic motion over the entire lobe once the particle finds and encounters the passage across the equatorial plane. All of the mentioned cases are illustrated in Fig. 17.

Increasing the energy further to  $\tilde{E} = 0.857$ , we obtain a broad potential lobe which almost touches the star surface. The situation changes from the previous case where the gate connecting the off-equatorial lobes was narrow. Now we do not find trajectories which occupy only one part of the lobe, above (or below) the equatorial plane. Chaotic trajectories densely filling the entire lobe are typical for this setup. We also encounter perfectly regular trajectories forming ribbon-like structures spanned between northern and southern borders of the lobe. In Poincaré sections these appear as regular islands surrounded by a chaotic ocean (upper panels of Fig. 18). We notice that the RP of this regular trajectory is extraordinarily simple and consists of almost perfect diagonal lines (bottom panels of Fig. 18). Thus its dynamic properties are close to those of a periodic system, which is in contrast with the neighboring fully chaotic orbits.

The second type (class IIa) of the effective potential topology of off-equatorial lobes differs from the first one



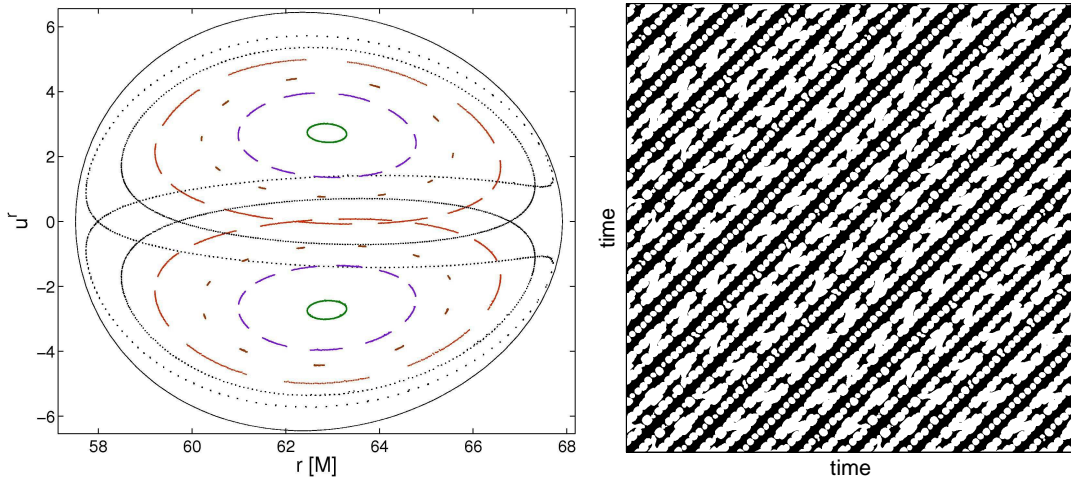


**Figure 19.** Regular motion in an off-equatorial lobe of the third type. Parameters used:  $\tilde{E} = 0.99579$ ,  $\tilde{L} = 6.25382 M$ ,  $\tilde{q}M = 45.87368 M^2$ ,  $\tilde{L} = 6.25382 M$ ,  $\Omega = 0.011485 M^{-1}$ . Particles are launched from latitude  $\theta(0) = \theta_{\text{section}} = 1.0492$ .

significantly as the lobes do not open towards the star when the energy is raised sufficiently. On the contrary, in this case we observe that the lobe's boundary touches the light cylinder first.

The motion in the off-equatorial lobes proves to be regular while the merging lobes bring chaos into play. Chaos becomes dominant for broader lobes, however, stable regular orbits also persist. The results are similar to those of the first type of potential topology discussed above.

The last analyzed topology of the lobes (class IIIc) differs profoundly from the preceding two cases, as can be seen in Fig. 15. We find that stable motion dominates in this setup. This can be verified by comparison with Fig. 19.

As we further increase the energy level, we obtain more complicated shapes of the equipotentials that allow the particle to fall on the star surface. On the other hand, opening the outflow gate energetically precedes the merging point of both off-equatorial lobes. In Fig. 20, we discuss the motion governed by the largest possible lobe which almost touches the light cylinder. We observe that stable regular orbits are still possible for those particles that do not hit the passage.

From the above-given discussion we conclude that the motion of charged test particles in the off-equatorial lobes allowed by the test field of the rotating magnetic dipole on the Schwarzschild background is largely regular. Once the off-equatorial lobes merge with each other, chaos may appear. Increasing the energy, the chaotic motion becomes typical but, quite surprisingly, very stable orbits also exist under these circumstances.

## 6. DISCUSSION AND CONCLUSIONS

We studied the regular and chaotic motion of electrically charged particles near a magnetized rotating black hole or a compact star. We employed the method of recurrence analysis in the phase space, which allowed us to characterize the chaoticness of the system in a quantitative manner. Unlike the method of Poincaré surfaces, the Recurrence Plots have not yet been widely used to study the chaotic systems in the regime of strong gravity.

The main motivation for these investigations is the question of whether the matter around magnetized compact objects can exhibit chaotic motion, or if instead the

system is typically regular. One of the main applications of our considerations concerns the putative envelopes of charged particles enshrouding the central body in a form of a fall-back corona, or plasma coronae extending above the accretion disk. While we concentrated on the specifications of the RP method in circumstances of a relativistic system, the assumed model cannot be considered as any kind of a realistic scheme for a genuine corona. We simply imposed a large-scale ordered magnetic field acting on particles in a combination with strong gravity.

Various aspects of charged particle motion were addressed throughout this paper. First of all, we investigated the motion in off-equatorial lobes above the horizon of a rotating black hole (modeled by Kerr metric equipped with the Wald test field), as well as above the surface of a magnetic star (modeled by the Schwarzschild metric with the rotating dipolar magnetic field). In both cases we conclude that the motion of test particles is regular, which was confirmed for a representative number of orbits across the wide range of parameters over all topological types of off-equatorial potential wells. This result is somewhat unexpected because the off-equatorial orbits require a perturbation to be strong enough (in terms of strength of the electromagnetic field), so that it can balance the vertical component of the gravitational force.

Further, we investigated the response of the particle dynamics when the energy level  $\tilde{E}$  was raised gradually from the potential minimum to values allowing cross-equatorial motion. We examined various topological classes of the effective potential and came to the conclusion that the cross-equatorial orbits are typically chaotic, although very stable regular orbits may also persist for a certain intermediate energy range. The classical work of Hénon & Heiles (1964) should be recalled in this context since it also identifies the energy as a trigger for chaotic motion in the analysed simple system. More recently the Hénon–Heiles system was revisited in the relativistic context by Vieira & Letelier (1996).

We also addressed the question of spin dependence of the stability of motion for Kerr black hole in the Wald field. We noticed that this is a rather subtle problem. The effective potential is by itself sensitive to the spin value  $a$  – hence, we had to link the potential value roughly linearly with the energy  $\tilde{E}$  to maintain the po-

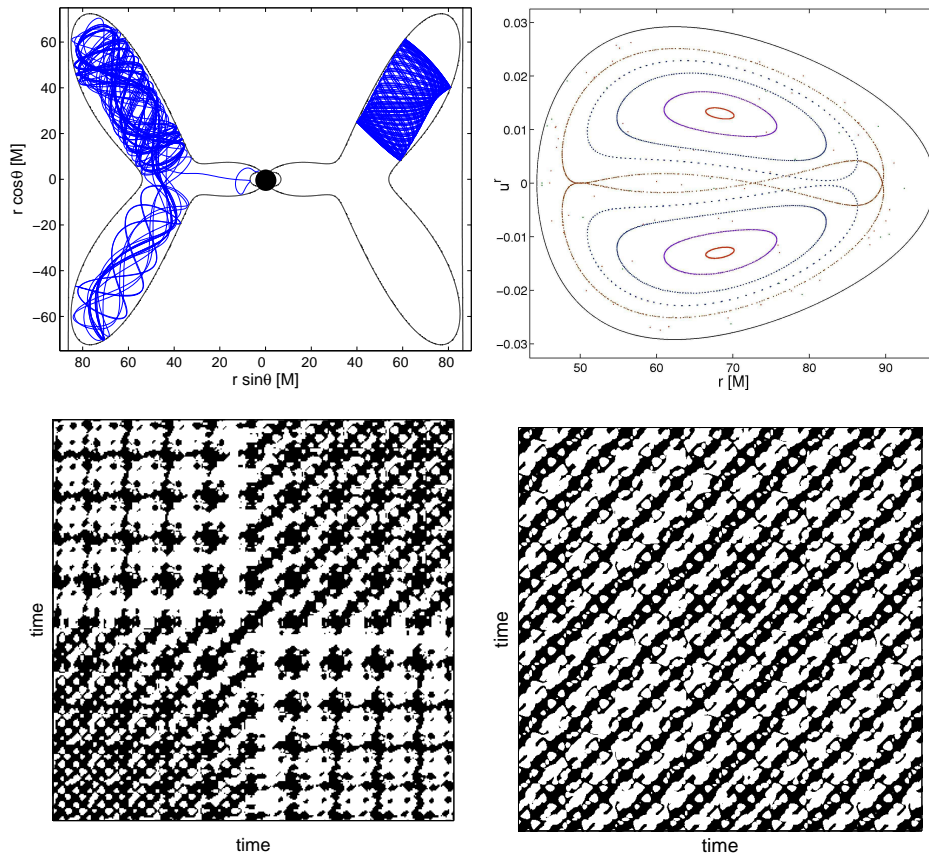


**Figure 20.** For the energy level  $\tilde{E} = 0.9962$  (other parameters as in Fig. 19) we obtain a large lobe that almost touches the light cylinder and allows the particle to fall onto the surface of the star via a narrow passage above and below the equatorial plane. The upper left panel shows two trajectories launched from  $\theta(0) = 1.0497$ ,  $u^r(0) = 0$ . One of the particles (starting from  $r(0) = 61.5 M$ ) follows an unstable path and eventually falls on the star surface. On the contrary, the other particle (starting from  $r(0) = 72.5 M$ ) moves regularly and never escapes any given part of the lobe. The upper-right panel shows these two kinds of trajectory depicted in the Poincaré surface of section. Chaotically dispersed points belong to the escaping trajectory. The bottom-left panel shows the Recurrence Plot of the escaping particle; this plot does not exhibit typical chaotic behavior, although the large-scale structures are present. The bottom-right panel presents the Recurrence Plot of stable motion.

tential lobe at a given position. In other words, we did not find any clear and unique indication of the spin dependence of the motion chaoticness. Most trajectories exhibited regular behavior, which is also in agreement with the previous results indicating that motion in off-equatorial lobes is generally regular. On the other hand, in the case of the cross-equatorial motion we observed that, for higher spins, more chaotic features come into play when compared with the case of slow rotation. This trend might be also attributed to simultaneous adjustments of  $\tilde{E}$ . In other words, it appears impossible to give an unambiguous conclusion about the spin dependence of the particles dynamics. Instead, one has to deal with a complex, interrelated dependence.

In the case of a Kerr black hole immersed in a large-scale magnetic field, we observed the effect of confinement of particles regularly oscillating around the equatorial plane. Escape of particles from the plane is allowed for a given range of initial conditions since the equipotentials do not close; they form an endless axial “valley” instead. The escaping trajectories create a narrow, collimated structure parallel to the axis.

Asking the question about the dynamical properties of motion of matter in the black hole corone is of theoretical interest by its own, but it is relevant also in view of precise spectroscopical and timing studies with

the forthcoming X-ray satellites. However, one more word of caution is appropriate especially concerning our assumption of the ordered magnetic field. Although the large-scale magnetic fields are adequate to describe the initial background field of the magnetic star or a toroidal current in the accretion disk (Koide et al. 2006; Beckwith et al. 2008; Rothstein & Lovelace 2008, e.g.), a turbulent component is known to develop quickly in the accreted plasma (McKinney & Narayan 2007). These will also perturb the motion of matter, and so the regular orbits may quickly disappear. This should translate to the transient emergence and subsequent disappearance of the periodic component in the observed signal.

We thank Dr. Tomáš Pecháček for helpful advice concerning the recurrence analysis, and Dr. Kendrah Murphy for her critical comments and useful suggestions. OK acknowledges the doctoral student program of the Czech Science Foundation (project No. 205/09/H033). JK, VK and ZS thank the Czech Science Foundation (No. P209/10/P190, 205/07/0052 and 202/09/0772). Astronomical Institute and the Institute of Physics have been operated under the projects MSM AV0Z10030501 and 4781305903, and further supported by the Ministry of Education project of Research Centres LC06014 in the Czech Republic.

## APPENDIX

## CHOICE OF PREFERRED OBSERVERS

When analyzing the dynamics in the general relativistic context the fundamental question arises whether the distinction between chaotic and regular motion is coordinate dependent or not. To this end Motter (2003) infers the transformation law for Lyapunov exponents. He concludes that although the Lyapunov exponents themselves are not invariant they transform in such a way that positive Lyapunov exponents remain positive and vice versa. In other words the distinction between regular and chaotic dynamics may be drawn invariantly.

In order to give the notion of recurrence a rigorous and, at the same time, an intuitive sense, we can employ the 3 + 1 formalism (Thorne & MacDonald 1982) that is based on an appropriate selection of a family of spacetime-filling three-dimensional spacelike hypersurfaces (foliation) of constant time  $t$ . The timelike curves orthogonal (in a spacetime sense) to the hypersurfaces may be regarded as the world-lines of a family of fiducial observers (FIDO) who naturally parameterize their world line by proper time  $\tau$  (whose rate of change generally differs from that of  $t$ ). FIDO identify each spatial hypersurface along his world line as a slice of simultaneity. The geometry of this spacetime slice is given by 3-metric  $\gamma_{ij}$ :

$$\gamma_{ij} = g_{ij} + u_i u_j, \quad (\text{A1})$$

where  $u_i$  stands for the spatial part of FIDO's four-velocity and  $g_{ij}$  for the spatial part of the spacetime metric. Considering also the time coordinate,  $\gamma_{\mu\nu}$  can be regarded as a projector onto the three-dimensional spatial hypersurface.

We select zero-angular momentum observers (ZAMO) (Bardeen et al. 1972) as an appropriate representation of the fiducial observers. Their orthonormal tetrad is given by

$$e_{(t)} = u = \frac{\sqrt{A}}{\sqrt{\Delta}\rho} \left( \frac{\partial}{\partial t} + \Omega \frac{\partial}{\partial \phi} \right) \quad (\text{A2})$$

$$e_{(r)} = \frac{\sqrt{\Delta}}{\rho} \frac{\partial}{\partial r} \quad (\text{A3})$$

$$e_{(\theta)} = \frac{1}{\rho} \frac{\partial}{\partial \theta} \quad (\text{A4})$$

$$e_{(\phi)} = \frac{\rho}{\sqrt{A} \sin \theta} \frac{\partial}{\partial \phi}, \quad (\text{A5})$$

where  $A \equiv (r^2 + a^2)^2 - a^2 \Delta \sin^2 \theta$  and  $\Omega = 2aA^{-1}Mr$ .

Projecting an arbitrary four-vector  $C^\mu$  onto ZAMO's hypersurface of simultaneity directly results in the following 3-dimensional quantities,

$${}^{\text{3D}}C^i = \gamma^{ij} C_j = (C^r, C^\theta, \gamma^{\phi\phi} C_\phi), \quad (\text{A6})$$

$${}^{\text{3D}}C_i = \gamma_{ij} {}^{\text{3D}}C^j = (C_r, C_\theta, g_{\phi\phi} C^\phi); \quad (\text{A7})$$

here,  $\gamma_{\phi\phi} = g_{\phi\phi}$  ( $u_\phi = 0$  for ZAMO) and, consequently,  $\gamma^{\phi\phi} g_{\phi\phi} = 1$ .

ZAMO tetrad components  ${}^{\text{3D}}C^{(i)}$  are given as

$${}^{\text{3D}}C^{(i)} = {}^{\text{3D}}C_{(i)} = e_{(i)j} {}^{\text{3D}}C^j \equiv (\sqrt{g_{rr}} C^r, \sqrt{g_{\theta\theta}} C^\theta, \sqrt{g_{\phi\phi}} C^\phi). \quad (\text{A8})$$

The hypersurface components of the phase space constituents  $x^i$  and  $\pi_i$ , as measured by ZAMO, are then:

$${}^{\text{3D}}x^{(i)} = (\sqrt{g_{rr}} r, \sqrt{g_{\theta\theta}} \theta, \sqrt{g_{\phi\phi}} \phi), \quad (\text{A9})$$

$${}^{\text{3D}}\pi_{(i)} = \left( \sqrt{g^{rr}} \pi_r, \sqrt{g^{\theta\theta}} \pi_\theta, \frac{1}{\sqrt{g_{\phi\phi}}} L \right). \quad (\text{A10})$$

The spatial 3-metric is

$$ds^2 = \delta_{(i)(j)} dx^{(i)} dx^{(j)} + O(|x^{(k)}|^2) dx^{(i)} dx^{(j)}, \quad (\text{A11})$$

where  $x^{(k)}$  represents the spatial distance from the origin of the tetrad, i.e. ZAMO's current location. ZAMO is not an inertial observer, which generally causes the first order corrections  $O(|x^{(k)}|)$  to the Minkowskian metric  $g_{(i)(j)} = \eta_{(i)(j)}$ . But these do not enter the spatial part of the metric. Thus the 3-metric within the spatial hypersurface is a Euclidean one, with the deviations of second order in the distance from the spatial origin on ZAMO's world-line.

We will use ZAMO's metric at distances up to the value of the threshold parameter  $\varepsilon$ . The Euclidean metric according to eq. (A11) will be therefore justified if  $\frac{\varepsilon^2}{P^2} \ll 1$ , where  $P$  stands for a constant (for a given ZAMO).  $P$  has the dimension of length and characterizes the curvature of the hypersurface. We suggest setting  $P \equiv K^{-1/4}$ , where  $K = R^{\mu\nu\xi\pi} R_{\mu\nu\xi\pi}$  represents the Kretschmann scalar evaluated from the Riemann curvature tensor. In the case

of the Kerr black hole the Kretschmann scalar may be expressed in a surprisingly simple form (Henry 2000). While constructing the Recurrence Plots, we check whether the condition  $\frac{\epsilon^2}{P^2} \ll 1$  remains satisfied.

The above-mentioned adoption of preferred observers is needed in order to maintain an operational criterion of chaos and be able to formulate an explicit form of the equations for RQA measures in a curved spacetime. Here the notion of the phase space distance plays a role. In Kerr metric (or another axially symmetric stationary spacetime), Fiducial Observers (a.k.a. FIDOs) represent a natural selection of preferred observers. Obviously, this option is not unique, and so a detailed appearance of the recurrence plots is also ambiguous to certain extent. But not so the main conclusions that we infer regarding the chaoticness versus regularity of the system behavior, because this distinction can be eventually traced down to the exponential versus polynomial growth of the separation with the particle proper time along neighboring trajectories.

We can deduce the kind of transformation between different families of observers that could affect our conclusions: these are transformations involving exponential dependencies on observer's phase-space position. For example transformation to accelerated frames and spacetime points in the vicinity of singularities may need a special consideration, as well as the investigation of highly dynamical spacetimes that are lacking symmetries. On the other hand, selecting LNRF to define ZAMOs in (weakly perturbed) Kerr metric outside the black hole horizon appears to be a well-substantiated choice.

Similar arguments for the adoption of preferred observers on the basis of spacetime symmetries have been elaborated in greater detail by Karas & Vokrouhlický (1992) in the context of Ernst's magnetized black hole, which is another particularly simple (static) exact solution of Einstein-Maxwell equations exhibiting the onset of chaos as the magnetic field strength is increased.

## REFERENCES

- Abramowicz, M. A., Nurowski, P., & Wex, N. 1995, *Classical Quant. Grav.*, 12, 1467
- Aliev, A. N., & Özdemir, N. 2001, *MNRAS*, 336, 241
- Bahcall, S., Lynn, B. W., & Selipsky, S. B. 1989, *Nucl. Phys. B*, 325, 606
- Bakala, P., Šrámková, E., Stuchlík, Z., & Török, G. 2010, *Classical Quant. Grav.*, 27, 045001
- Bardeen, J. M., Press, W. H., & Teukolsky, S. A. 1972, *ApJ*, 178, 347
- Beckwith, K., Hawley, J. F., & Krolik, J. H. 2008, *ApJ*, 678, 1180
- Bičák, J., Stuchlík, Z., & Balek, V. 1989, *Bull. Astron. Inst. Czechoslovakia*, 40, 65
- Bisnovatyi-Kogan, G. S., & Lovelace, R. V. E. 2007, *ApJ*, 667, L167
- Carter, B. 1968, *Phys. Rev.*, 174, 1559
- Casares, J. 2007, in *Black Holes from Stars to Galaxies – Across the Range of Masses*, Proc. IAU Symposium 238, eds. V. Karas & G. Matt (Cambridge: Cambridge University Press), p. 3
- Czerny, B., & Nikolajuk, M. 2010, *Mem. Soc. Astron. Italiana*, 81, 281
- de Felice, F. 1979, *Phys. Lett. A*, 69, 307
- Eckmann, J. P., Oliffson, K. S., & Ruelle, D. 1987, *Europhys. Lett.*, 5, 973
- Glendenning, N. K. 1997, *Compact Stars. Nuclear Physics, Particle Physics, and General Relativity* (Berlin: Springer)
- Hénon, M., & Heiles, C. 1964, *AJ*, 69, 73
- Henry, R. C. 2000, *ApJ*, 535, 350
- Karas, V., & Vokrouhlický, D. 1992, *Gen. Relat. Gravit.*, 24, 729
- Koide, S. 2004, *ApJ*, 606, L45
- Koide, S., Kudoh, T., & Shibata, K. 2006, *Phys. Rev. D*, 74, 044055
- Kovář, J., Kopáček, O., Karas, V., & Stuchlík, Z. 2010, *Classical Quant. Grav.*, 27, 135006
- Kovář, J., & Stuchlík, Z. 2007, *Classical Quant. Grav.*, 24, 565
- Kovář, J., Stuchlík, Z., & Karas, V. 2008, *Classical Quant. Grav.*, 25, 095011
- Lichtenberg, A. J., & Leiberman, M. A. 1992, *Regular and chaotic dynamics* (New York: Springer)
- Lipunov, M. M. 1992, *Astrophysics of Neutron Stars, Astronomy and Astrophysics Library* (New York: Springer)
- Lukes-Gerakopoulos, G., Apostolatos, T. A., & Contopoulos, G. 2010, *Phys. Rev. D*, 81, 124005
- Marwan, N., Carmen Romano, M., Thiel, M., & Kurths, J. 2007, *Physics Rep.*, 438, 237
- McKinney, J. C., & Narayan, R. 2007, *MNRAS*, 375, 531
- Mestel, L. 1999, *Stellar Magnetism* (Oxford: Clarendon Press)
- Miller, J. C., Shahbaz, T., & Nolan, L. A. 1998, *MNRAS*, 294, L25
- Misner, C. W., Thorne, K. S., & Wheeler, J. A. 1973 *Gravitation* (San Francisco: Freeman)
- Motter E. M. 2003, *Phys. Rev. Lett.*, 91, 231101
- Murphy, K., Yaqoob, T., Karas, V., & Dovčiak, M. 2009, *ApJ*, 701, 635
- Nakamura, Y., & Ishizuka, T. 1993, *Astrophys. Space Sci.*, 210, 105
- Narayan, R. 2005, *New J. Phys.*, 7, 199
- Neukirch, T. 1993, *A&A*, 274, 319
- Petterson, J. A. 1975, *Phys. Rev. D*, 12, 2218
- Podolský, J., & Veselý, K. 1998, *Phys. Rev. D*, 58, 081501
- Prasanna, A. R. 1980, *Nuovo Cimento, Rivista*, 3, 1
- Prasanna, A. R., & Sengupta, S. 1994, *Phys. Lett. A*, 193, 25
- Preti, G. 2010, *Phys. Rev. D*, 81, 024008
- Punsly, B. 2008, *Black Hole Gravitohydrodynamics* (Berlin: Springer)
- Reynolds, C. S., & Nowak, M. 2003, *Phys. Rep.*, 377, 389
- Rothstein, D. M., & Lovelace, R. V. E. 2008, *ApJ*, 677, 1221
- Semerák, O., & Suková, P. 2010, *MNRAS*, 404, 545
- Sengupta, S. 1995, *ApJ*, 449, 224
- Skokos, Ch. 2010, in *Dynamics of Small Solar System Bodies and Exoplanets*, ed. J. Souchay and R. Dvorak, *Lect. Notes Phys.* 790 (Springer: Berlin), p. 63
- Stuchlík, Z., Bičák, J., & Balek, V. 1999, *Gen. Relat. Gravit.*, 31, 53
- Stuchlík, Z., Török, G., Hledík, S., & Urbanec, M. 2009, *Classical Quant. Grav.*, 26, 035003
- Takahashi, M., & Koyama, H. 2009, *ApJ*, 693, 472
- Takens, F. 1981, *Lect. Notes Math.* 898, 366
- Thiel, M., Romano, M. C., & Kurth, J. 2004, *Phys. Lett. A*, 330, 343
- Thiel, M., Romano, M. C., Read, P. L., & Kurths, J. 2004, *Chaos*, 14, 234
- Thorne, K. S., & MacDonald, D. 1982, *MNRAS*, 198, 339
- Tomimatsu, A., & Takahashi, M. 2001, *ApJ*, 552, 710
- Trulla, L. L., Giuliani, A., Zbilut, J. P., & Webber, Jr., C. L. 1996, *Phys. Lett. A*, 223, 255
- Vestergaard, M. 2010 in *Proc. of IAU Symposium 267: Evolution of Galaxies and Central Black Holes: Feeding and Feedback*, eds. Peterson, B., Somerville, R., & Storchi-Bergmann, T. (Cambridge: Cambridge University Press)
- Vieira, W. M., & Letelier, P. S. 1996, *Phys. Rev. Lett.*, 76, 1409
- Wald, R. M. 1974, *Phys. Rev. D*, 10, 1680
- Yoshida, H. 1993, *Celest. Mech. Dyn. Astr.*, 56, 27